A fully three-dimensional model of interpenetrating collagen fibrillar networks for intervertebral disc mechanics

Abderrahman Tamoud, Fahmi Zaïri, Amar Mesbah, Fahed Zaïri

Version of Record: https://www.sciencedirect.com/science/article/pii/S0020740322002247
Manuscript_2fcfd1e79d4d939965dfb23981a544c5

A fully three-dimensional model of interpenetrating collagen fibrillar networks for intervertebral disc mechanics

Abderrahman Tamoud[a,b], Fahmi Zaïri[a*], Amar Mesbah[b], Fahed Zaïri[c]

[a]Lille University, Civil Engineering and geo-Environmental Laboratory (ULR 4515 LGCgE), 59000 Lille, France
[b]University of Sciences and Technology Houari Boumediene, Laboratory of Advanced Mechanics, 16111 Algiers, Algeria
[c]Ramsay Générale de Santé, Hôpital privé Le Bois, 59000 Lille, France

*Corresponding author.
E-mail address: fahmi.zairi@polytech-lille.fr

Abstract

In this work, a fully three-dimensional model of the human intervertebral disc is proposed within a purely analytical framework in the final goal to create time and cost-efficient patient-specific models. The constitutive representation considers the deformation-induced damage along with the hydration effects on the regional disc mechanics. Special functions are introduced to generate versatile and anatomically accurate disc geometries taking into account morphology regional variation. The complex interpenetrating collagen fibrillar networks are explicitly introduced in the three-dimensional model considering the regional variation throughout the disc. A quantitative evaluation of the predictive capabilities of a human lumbar disc model shows a good agreement with compression and torsion experiments from the literature both for the overall disc stiffness and for the direct MRI kinematic fields. Model predictions are then performed and critically discussed on axially/torsionally loaded human lumbar discs.

Keywords: Full disc model; Multiscale structure; Regional variation; Nucleus-annulus interaction.

1. Introduction

At the start of the new millennium, the creation of digital twins of human organs has become a priority for the completion of predictive medicine [1-5]. The intervertebral disc of the human spine is probably one of the most extraordinary heterogeneous material system that the nature produces. Its complex structural organization of interpenetrating collagen fibrillar networks has been only revealed and appreciated recently [6-7]. The disc presents a hierarchical lamellar structure in which nano-sized elastic fibers (NEF) connect both two micro-sized type-I oriented collagen fibers (OCF) of the concentric lamellae (LM) and two

adjacent LM between them by crossing the inter-lamellar (ILM) ground matrix. Besides, the regional variation in organization of collagen fibrillar networks throughout the disc leads to a heterogeneous mechanics of the disc [8-9]. These recent discoveries about relationship between interpenetrating collagen fibrillar networks and disc mechanics are still not taken into consideration in the current quantitative predictions. The physically realistic constitutive representation of the disc soft tissues remains the prerequisite of any relevant predictive tool. It allows to offer a quantitative prediction but also a deeper understanding of the separate and synergistic effects of the hierarchical structural features, from nano-sized fibers to micro-sized concentric lamellae, that govern the disc macro-response. Such a predictive tool would provide a deeper understanding of the origin of the deformation-induced damage mechanisms affecting the disc functionality.

A short overview of the literature shows that a lot of disc models have been proposed over the years, to name a few [10-23]. Beyond the fact that all existing disc models are most naturally modeled using the finite element method, their main distinction lies in the constitutive representation done for the structure-mechanical relationship of the disc soft tissues. While the OCF network is commonly introduced in the current disc models, the interpenetrating NEF network is still largely unappreciated and neglected. The consideration of the collagen fibrillar networks in disc modeling strategies is nonetheless essential for an accurate prediction of the local and overall disc responses. Besides, to reflect the real disc mechanics, any model should also consider variations of the disc shape and size with the spinal level and age [24-26], the disc hydration state [27-28], the disc volume change under applied loadings [22] and the disc health state [29-31]. All the latter aspects are very attractive in the aim to create patient-specific models taking into account realistic structure/macrostructure features of each patient. Moreover, in order to provide quantitive predictions of the disc health and the risk of injuries, the constitutive representation of the disc must integrate the damage-induced functionality loss leading to more vulnerability regarding to the external mechanical loadings.

The main objective of this work is to formulate a fully three-dimensional model of the whole human disc while taking into account the most recent discoveries about interpenetrating collagen fibrillar networks along with relationship to mechanics. The constitutive model proposed in our previous contributions [9, 32] to capture the damage-hydration effects on the annulus fibrosus mechanics are here further developed in order to provide a new model of the whole human disc. The latter is developed within a purely analytical framework in the final goal to create time and cost-efficient patient-specific models of the human disc predicting the microstructure-shape-mechanics relationship. Contrary to the existing models in the current

state-of-the-art, the present model provides a fully three-dimensional realistic description of the multiscale structure in terms of lamellar-interlamellar connection and interpenetrating collagen fibrillar distribution while accounting combined damage-hydration effects. The proposed modeling approach is based on a new and direct analytical method for the creation of discs allowing versatile possibilities of regional-dependent geometry variations. This contribution provides the detailed mathematical developments of the disc model. Some predictive results are presented to illustrate the model capacities under axial/torsion loading modes, especially regarding the disc heterogeneous mechanics.

The outline of the present paper is as follows. Section describes the theory considering general assessments of the tube-like solid mechanics along with specifities regarding disc structure and macrostructure. Predictions are presented and discussed in Section 3. Section 4 closes the paper with concluding remarks.

The following notation is used throughout the text. Tensors and vectors are respectively denoted by normal boldfaced letters and italicized boldfaced letters, while scalars and individual components of vectors and tensors are denoted by normal italicized letters. The superposed dot designates the time derivative.

2. Model

2.1. Tube-like kinematics

This subsection provides the kinematics framework of the tube-like solid mechanics. The general theory was originally developed for elastomeric-like material cylinders [33-35] and arterial walls [36]. Some adaptations to discs are here brought in the kinematics especially considering regional variations in morphology and in structure-property relationships. Combined axial/torsion loadings at the external boundary of the disc will be considered in the present theoretical developments as illustrated in Figure 1. An internal pressure simulating the nucleus swelling may be activated when the compression is considered [37-38]. The nucleus is referred as the central portion i = 0 and the annulus is seen as a multi-layered tube divided into n rings $i = 1, \ldots n$. The half-disc topology is provided in Figure 2 in superior and sagittal views.

In the initial configuration, the solid is referenced in cylindrical polar coordinates (R, Θ, Z):

$$R^i \in \left[R^i_{inner}, R^i_{outer} \right], \ \Theta \in [0, 2\pi] \ \text{ and } \ Z^i \in \left[0, H^i \right] \tag{1}$$

where R^i_{inner} and R^i_{outer} denote the initial inner and outer radii of each ring, respectively, and H^i is the initial height. These anatomical features vary from a region to another according to the circumferential axe $\boldsymbol{\Theta}$.

The kinematics of an axially/torsionally loaded tube-like solid is given as follows [33-36]:

$$r^i = f^i\left(R^i,\, r^{i-1}\right),\ \theta = \Theta + \frac{\varphi}{H^i} Z^i \quad \text{and} \quad z^i = \lambda^i_z Z^i \tag{2}$$

with

$$r^i \in \left[r^i_{inner}, r^i_{outer}\right],\ \theta \in [0, 2\pi] \text{ and } z^i \in \left[0, h^i\right] \tag{3}$$

In the present work, r^i_{inner} and r^i_{outer} denote the current inner and outer radii of each ring, respectively, and h^i is the current height. The term φ is the twist angle of the disc arising from the torsion and λ^i_z is the axial stretch applied in the z-axis. The quantity f^i is a function dependent on the initial radius R^i of the ring i and the current radius r^{i-1} of the adjacent ring $i-1$.

The deformation gradient tensor $\mathbf{F}^i$ of each ring may be thus written as [33, 36]:

$$\mathbf{F}^i = \frac{\partial r^i}{\partial R^i} \boldsymbol{e}_r \otimes \boldsymbol{E}_r + \frac{r^i}{R^i}\frac{\partial \theta}{\partial \Theta} \boldsymbol{e}_\theta \otimes \boldsymbol{E}_\theta + r^i \frac{\partial z^i}{\partial Z^i}\frac{\partial \theta}{\partial z^i} \boldsymbol{e}_\theta \otimes \boldsymbol{E}_z + \frac{\partial z^i}{\partial Z^i} \boldsymbol{e}_z \otimes \boldsymbol{E}_z \tag{4}$$

where $\{\boldsymbol{E}_r,\ \boldsymbol{E}_\theta,\ \boldsymbol{E}_z\}$ and $\{\boldsymbol{e}_r,\ \boldsymbol{e}_\theta,\ \boldsymbol{e}_z\}$ are the unit vectors in the initial and current configurations, respectively.

The chemical-induced volumetric effects are also introduced via a chemo-mechanical coupling considering the multiplicative decomposition concept and the introduction of an intermediate configuration. The total deformation $\mathbf{F}^i = \mathbf{F}^i_{chem} \cdot \mathbf{F}^i_{mech}$ is decomposed into chemical-induced volumetric and mechanical parts $\mathbf{F}^i_{chem}$ and $\mathbf{F}^i_{mech}$.

The chemical deformation gradient tensor $\mathbf{F}^i_{chem}$ is expressed in each ring as follows:

$$\mathbf{F}^i_{chem} = \lambda^i_{chem\_r} \boldsymbol{e}_r \otimes \boldsymbol{E}_r + \lambda^i_{chem\_\theta} \boldsymbol{e}_\theta \otimes \boldsymbol{E}_\theta + \lambda^i_{chem\_z} \boldsymbol{e}_z \otimes \boldsymbol{E}_z \tag{5}$$

where $\lambda^i_{chem\_r}$, $\lambda^i_{chem\_\theta}$ and $\lambda^i_{chem\_z}$ are the chemical stretches along the three polar directions $\boldsymbol{r}$, $\boldsymbol{\theta}$ and z, respectively.

Using Eqs. (3) to (4), the mechanical deformation gradient tensor $\mathbf{F}^i_{mech}$ may be expressed as:

$$\mathbf{F}^i_{mech} = \frac{\partial r^i}{\partial R^i}\frac{1}{\lambda^i_{chem\_r}} \boldsymbol{e}_r \otimes \boldsymbol{E}_r + \frac{r^i}{R^i}\frac{1}{\lambda^i_{chem\_\theta}} \boldsymbol{e}_\theta \otimes \boldsymbol{E}_\theta + \frac{r^i \varphi}{H}\frac{1}{\lambda^i_{chem\_\theta}} \boldsymbol{e}_\theta \otimes \boldsymbol{E}_z + \frac{\lambda_z}{\lambda^i_{chem\_z}} \boldsymbol{e}_z \otimes \boldsymbol{E}_z \tag{6}$$

The overall deformation gradient tensor $\mathbf{F}_{annulus}$ in the annulus may be calculated using a volume-weighted average of the LM deformations $\mathbf{F}^{LM\_i} = \mathbf{F}_{chem}^{LM\_i}.\mathbf{F}_{mech}^{LM\_i}$ and the ILM deformations $\mathbf{F}^{ILM\_i} = \mathbf{F}_{chem}^{ILM\_i}.\mathbf{F}_{mech}^{ILM\_i}$ [39]:

$$\mathbf{F}_{annulus} = \sum_{i=1,3...}^{n} \phi_{ring\_0}^{i} \mathbf{F}^{LM\_i} + \sum_{i=2,4...}^{n-1} \phi_{ring\_0}^{i} \mathbf{F}^{ILM\_i} \tag{7}$$

in which $\phi_{ring\_0}^{i}$ is the initial volume fraction of a ring i.

2.2. Annulus-nucleus interaction

2.2.1. Nucleus swelling

When the disc is subjected to a compression, the nucleus swells (Figure 1). The latter may be introduced thanks to the chemical deformation gradient $\mathbf{F}_{chem}^{0}$ in the nucleus:

$$\mathbf{F}_{chem}^{0} = \left(1 + \xi\chi\right)\mathbf{I} \tag{8}$$

where ξ is the chemical expansion at the equilibrium state and χ is a function of time $\chi = 1 - \exp\left(-t/\tau\right)$ in which τ is the chemical expansion rate.

After a series of straightforward derivations, the nucleus actual radius r^0 is given by:

$$r^0 = \sqrt{\left(R^0\right)^2 \frac{\varepsilon_{chem}^{0} + 1}{\lambda_z^0}} \tag{9}$$

in which $\varepsilon_{chem}^{0} = \det\left(\mathbf{F}_{chem}^{0}\right) - 1$ is the chemical-induced volumetric strain in the nucleus with $\det\left(\mathbf{F}_{chem}^{0}\right) > 0$ the Jacobian of the deformation gradient tensor $\mathbf{F}_{chem}^{0}$.

2.2.2. Annulus swelling

The annulus volumetric change due to the internal fluid variation is expressed by the chemical deformation gradient $\mathbf{F}_{chem}^{i}$. Considering fluid diffusivity anisotropy in annulus, the latter is given by [39]:

$$\mathbf{F}_{chem}^{i} = \mathbf{I} + \frac{2}{\sqrt{3}} \cos\alpha^{i} \operatorname{diag}\left(\xi_r^i \chi_r^i,\, \xi_\theta^i \chi_\theta^i,\, \xi_z^i \chi_z^i\right) \tag{10}$$

where ξ_r^i, ξ_θ^i and ξ_z^i are again chemical expansions at the equilibrium state and, χ_r^i, χ_θ^i and χ_z^i are again functions of time $\chi_{r,\theta,z}^{i} = 1 - \exp\left(-t/\tau_{r,\theta,z}^{i}\right)$ in which τ_r^i, τ_θ^i and τ_z^i are the chemical expansion rates. The term α^i denotes the OCF angle with respect to the circumferential direction of the disc.

After a series of straightforward derivations, the following expression is obtained for the function f^i using the continuity condition between the adjacent rings ($r^i_{inner} = r^{i-1}_{outer}$) and the mechanical incompressibility:

$$f^i = \sqrt{\left(\left(R^i_{inner,\,outer}\right)^2 - \left(R^i_{inner}\right)^2\right)\frac{\varepsilon^i_{chem}+1}{\lambda^i_z} + \left(r^{i-1}_{outer}\right)^2} \tag{11}$$

where $\varepsilon^i_{chem} = \det\left(\mathbf{F}^i_{chem}\right) - 1$ is the chemical-induced volumetric strain in the ring i.

The annulus is assembled by considering the effective interactions between adjacent layers via the compatibility conditions on the deformations $\mathbf{F}^i$ and on the Cauchy stresses $\boldsymbol{\sigma}^i$:

$$\mathbf{F}^{LM\_i}.\boldsymbol{n}^i_0 = \mathbf{F}^{ILM\_i+1}.\boldsymbol{n}^i_0 \text{ and } \boldsymbol{\sigma}^{LM\_i}.\boldsymbol{n}^i = \boldsymbol{\sigma}^{ILM\_i+1}.\boldsymbol{n}^i \tag{12}$$

where $\boldsymbol{n}^i_0$ and $\boldsymbol{n}^i$ are arbitrary unit vectors at the LM/ILM interfaces in the initial and current configurations, respectively.

In the absence of body loads, the equilibrium equations write as the spatial divergence of the overall Cauchy stress tensor $\boldsymbol{\sigma}$:

$$\mathrm{div}\left(\boldsymbol{\sigma}\right) = 0 \tag{13}$$

Considering the symmetry of the stress tensor $\boldsymbol{\sigma} = \boldsymbol{\sigma}^T$, Eq. (13) can be re-written using the stress components in the cylindrical coordinate system as follows:

$$\frac{\partial \sigma_{rr}}{\partial r} + \frac{1}{r}\frac{\partial \sigma_{r\theta}}{\partial \theta} + \frac{\partial \sigma_{rz}}{\partial z} + \frac{\sigma_{rr} - \sigma_{\theta\theta}}{r} \equiv \frac{\mathrm{d}\sigma_{rr}}{\mathrm{d}r} + \frac{\sigma_{rr} - \sigma_{\theta\theta}}{r} = 0 \tag{14}$$

From this equation and the boundary condition of the radial Cauchy stress $\sigma^i_{rr}\Big|_{r^i = r^n_{outer}} = 0$ on the outer wall of the last ring of the annulus, the internal pressure of the nucleus $\sigma_{nucleus} = -\sigma^i_{rr}\Big|_{r^i = r^1_{inner}}$ on the inner wall of the first ring of the annulus can be expressed dependent on θ direction in the form [36]:

$$\sigma_{nucleus} = 2\int_0^{\pi}\int_{r^1_{inner}}^{r^n_{outer}} \frac{\sigma^i_{\theta\theta} - \sigma^i_{rr}}{r^i}\,\mathrm{d}r^i\,\mathrm{d}\theta \tag{15}$$

2.3. Disc macrostructure

2.3.1. Disc geometry

As shown in the half-disc topology provided in Figure 2, we consider radial and circumferential variations of the geometry in order to propose anatomically accurate patient-specific models. For reasons of symmetry with respect to the sagittal plane of the disc, the

nucleus initial radius R^0 was defined by the following special mathematical function by an angle Θ between the anterior region ($\Theta = 0$) and the posterior region ($\Theta = \pi$) following the direction $\boldsymbol{\Theta}$ as illustrated in Figure 2:

$$R^0 = R^0_{frontal}\left[\left(1 + f_R - f_R f_\Theta\right)\left(1 - H_\Theta\right) + \left(f_R\left(\frac{f_\Theta^4 - 1}{f_\Theta(\pi) - 1}\right) + 1\right)H_\Theta\right] \tag{16}$$

in which H_Θ is the Heaviside function:

$$H_\Theta = 1 \quad \Theta > \frac{2\pi}{3} \text{ and } H_\Theta = 0 \quad \Theta \le \frac{2\pi}{3} \tag{17}$$

The function f_Θ is expressed as:

$$f_\Theta = \exp\left(-\left(\Theta - \frac{2\pi}{3}\right)^2\right) \tag{18}$$

The term f_R is a shape factor of the nucleus given by the ratio between the sagittal and frontal initial radii $R^0_{sagittal}$ and $R^0_{frontal}$:

$$f_R = \frac{R^0_{sagittal}}{R^0_{frontal}} - 1 \tag{19}$$

In the limit case $R^0_{sagittal} = R^0_{frontal}$, Eq. (16) becomes $R^0 = R^0_{frontal}$ and the disc has a circular basis.

The initial radius R^i in each ring is calculated as follows:

$$R^i_{outer} = R^0 + \sum_{k=1}^{i} \frac{t_k}{2} \tag{20}$$

in which t_k is the ring thickness. The continuity condition between the adjacent rings writtes $R^i_{inner} = R^{i-1}_{outer}$ (see Figure 2).

2.3.2. Thickness regional variation

The thicknesses of the LM and ILM layers are given by the following linear equations:

$$t_i^{LM} = a_t i + b_t \quad \text{for } i = 1,3,5...n \tag{21}$$

$$t_i^{ILM} = r_{ILM/LM} t_i^{LM} \quad \text{for } i = 2,4,6...n-1 \tag{22}$$

where $r_{ILM/LM}$ represents the thickness ratio of the ILM and LM zones and, a_t and b_t are functions expressed as:

$$a_t = \frac{(t_{PO} - t_{PI} + t_{AI} - t_{AO})\Theta + (t_{AO} - t_{AI})\pi}{(n-1)\pi} \tag{23}$$

$$b_t = \frac{(t_{PI} - t_{AI})\Theta + t_{AI}\pi}{\pi} - a \tag{24}$$

in which t_{PO}, t_{PI}, t_{AO} and t_{AI} are the regional ring thicknesses. The terms t_{AO} and t_{PO} denote the thicknesses for the outer side of the ring $i = n$, respectively, in the anterior region ($\Theta = 0$) and the posterior region ($\Theta = \pi$) whereas the terms t_{AI} and t_{PI} are their counterparts for the inner side of the ring $i = 1$. The linear interpolation is performed with an angular increment $\delta\theta$ of 1°. The same increment is fixed for all the other spatial discretizations in the circumferential direction. Note that the radial disctretization is fixed by the total number of layers n.

2.3.3. Height regional variation

The regional variation of the disc height is taken into account using the following linear equation:

$$H^i = a_H i + b_H \tag{25}$$

with

$$a_H = \frac{(H_{PO} + H_{AI} - H_{AO} - H_{PI})\Theta + (H_{AO} - H_{AI})\pi}{(n-1)\pi} \tag{26}$$

$$b_H = \frac{(H_{PI} - H_{AI})\Theta + H_{AI}\pi}{\pi} - a_H \tag{27}$$

in which H_{PO}, H_{PI}, H_{AO} and H_{AI} are the regional disc heights.

The final model takes into account the non-symmetry both in thickness and in height in order to propose anatomically accurate representations.

2.4. Disc structure

2.4.1. Constituents

As illustrated in Figure 3, the disc collagen fibrillar networks are decomposed into OCF and (inter-fibrillar and inter-lamellar) NEF both superimposed into the extracellular matrix (ECM). The volume fractions of these different solid constituents are calculated as follows:

$$\phi_{ECM} = \frac{\phi_{ECM\_0}}{\varepsilon_{chem} + 1}, \ \phi_{OCF} = \frac{\phi_{OCF\_0}}{\varepsilon_{chem} + 1} \text{ and } \phi_{NEF} = \frac{\phi_{NEF\_0}}{\varepsilon_{chem} + 1} \tag{28}$$

in which ϕ_{ECM_0}, ϕ_{OCF_0} and ϕ_{NEF_0} are the volume fractions at the chemical equilibrium state and, $\varepsilon_{chem} = \det\left(\mathbf{F}_{chem}\right) - 1$ is the chemical-induced volumetric strain. The volume fraction of the fluid phase ϕ_{fluid} corresponds to $\phi_{fluid} = 1 - \phi_{ECM} - \phi_{OCF} - \phi_{FCN}$.

The regional variation in quantities was taken into account using linear interpolations similar to those introduced above for the macrostructure features. Figure 3 provides the regional dependent quantities in the form of contour plots in the superior view of the disc.

2.4.2. Hierarchical fibrillar structure

The interpenetrating collagen fibrillar networks are spatially disposed in the model using two representative angles with respect to the global benchmark of the disc. The angles α^i are introduced to dispose the micro-sized OCF with respect to the circumferential direction of the disc with alternate orientations between successive lamellae. The angles ψ^i is introduced to dispose the nano-sized NEF network with respect to the radial direction in the OCF parallel plane.

The OCF in each LM ring is described geometrically by the unit vector $\boldsymbol{a}^i$ expressed, in the current configuration, with respect to the global benchmark of the disc:

$$\boldsymbol{a}^i = \cos\alpha^i\,\boldsymbol{\theta} + \sin\alpha^i\,\boldsymbol{z} \tag{29}$$

In order to introduce the change in the OCF angle induced by the circumferential stretch λ_θ, a measure of the reorientation may be considered geometrically using the following relation:

$$\alpha^i = \arctan\left(\frac{\lambda_\theta^i}{\lambda_z^i}\tan\alpha_0^i\right) \tag{30}$$

in which α_0^i is the OCF angle with respect to the circumferential direction of the disc in the initial configuration and λ_z^i is the axial stretch.

The unit vector $\boldsymbol{b}^i$ of each fibril is expressed, in the current configuration, with respect to the global benchmark of the disc as follows:

$$\boldsymbol{b}^i = \sin\psi^i\,\boldsymbol{r} + \cos\alpha\cos\psi^i\,\boldsymbol{\theta} + \sin\alpha^i\cos\psi^i\,\boldsymbol{z} \tag{31}$$

Again, the stretch-induced reorientation of the fibrils array is geometrically considered in each ring using the following expression:

$$\psi^i = \arctan\left(\left(1 - H\left(\psi_0^i - 90°\right)\right)\frac{\lambda_r^i}{\lambda_f^i}\tan\psi_0^i + H\left(\psi_0^i - 90°\right)\left(180° + \frac{\lambda_r^i}{\lambda_f^i}\tan\psi_0^i\right)\right) \tag{32}$$

in which ψ_0^i is the fibrils angle in the initial configuration, λ_r^i is the radial stretch and λ_f^i is the stretch in the OCF direction. The term $H(\bullet)$ is the Heaviside function.

The regional variation in network orientation was considered using linear interpolations with radial and circumferential variations as detailed in Appendix A. The collagen fibrillar organization is provided in Figure 4 in the form of contour plots in the superior view of the disc for the OCF network and in the form of contour plots in the sagittal view of the disc for the NEF network.

2.5. Constitutive equations

The local structure-mechanics relations are described using a recently developed fully three-dimensional constitutive model [9, 32]. In our previous works [9, 32], the model efficiencies to reproduce regional dependent multiaxial mechanics till failure of the human lumbar disc annulus were shown. In what follows, we present a summary of the constitutive equations of both healthy and damaged components.

2.5.1. Healthy components

In virtue of the chemo-mechanical coupling, the total free energy W is additively split into a mechanical part W_{mech} and a chemical part W_{chem}:

$$W = W_{mech} + W_{chem} \tag{33}$$

The mechanical free energy W_{mech} is obtained using as ensemble-volume averaged homogenization procedure a volume-weighted average of the different solid components:

$$W_{mech} = \phi_{OCF} W_\alpha + \sum_\psi \phi_\psi W_\psi + \phi_{ECM} W_{ECM} \tag{34}$$

in which W_α is the OCF free energy, W_ψ is the fibrils network free energy and W_{ECM} is the ECM free energy. The quantity $\phi_\psi = \phi_\eta \phi_{NEF}$ is the fibrils volume fraction calculated using the NEF volume fraction ϕ_{NEF} in a layer and the volume fraction of fibril bundles ϕ_η in a layer dependent on η with $\sum_\eta \phi_\eta = 1$.

The different free energies in Eq. (34) are expressed by considering both collagen fibrillar networks and ECM as hyperelastic bodies with isotropic, homogeneous and incompressible features. The free energies W_α and W_ψ may be expressed as a function of the fourth stretch

invariants $\overline{I}_{4\alpha} = \boldsymbol{a}.\mathbf{C}_{mech}.\boldsymbol{a} = \lambda_{\alpha}^{2}$ and $\overline{I}_{4\psi} = \boldsymbol{b}.\mathbf{C}_{mech}.\boldsymbol{b} = \lambda_{\psi}^{2}$ of the right Cauchy-Green deformation $\mathbf{C}_{mech} = \mathbf{F}_{mech}^{T}.\mathbf{F}_{mech}$. To describe the 'toe'-to-'linear' transition of the collagen response, two distinct relations are retained below and above $\lambda_{\alpha,\psi}^{*}$:

$$W_{\alpha,\psi} = H\left(\overline{I}_{4\alpha,\psi} - 1\right)\left[\frac{1}{2}\frac{C_1}{C_2}\left(\exp\left(C_2\left(\overline{I}_{4\alpha,\psi} - 1\right)^2\right) - 1\right)\right] \quad \lambda_{\alpha,\psi} < \lambda_{\alpha,\psi}^{*} \tag{35}$$

below $\lambda_{\alpha,\psi}^{*}$ and,

$$W_{\alpha,\psi} = H\left(\overline{I}_{4\alpha,\psi} - 1\right)\left[\frac{C_3}{2}\left(\overline{I}_{4\alpha,\psi} - \overline{I}_{4\alpha,\psi}^{*}\right)^2 + \zeta_{\alpha,\psi}\left(\overline{I}_{4\alpha,\psi} - \nu_{\alpha,\psi}\right)\right] \quad \lambda_{\alpha,\psi} \geq \lambda_{\alpha,\psi}^{*} \tag{36}$$

above $\lambda_{\alpha,\psi}^{*}$.

The terms C_1, C_2 and C_3 are material constants, $\overline{I}_{4\alpha,\psi}^{*}$ is the fourth stretch invariant for $\lambda_{\alpha,\psi} = \lambda_{\alpha,\psi}^{*}$, $H(\bullet)$ is the Heaviside function that ensures only stretching of the collagen and, $\zeta_{\alpha,\psi}$ and $\nu_{\alpha,\psi}$ are functions that ensure continuity between 'toe' and 'linear' regions:

$$\zeta_{\alpha,\psi} = C_1\left(\overline{I}_{4\alpha,\psi}^{*} - 1\right)\exp\left(C_2\left(\overline{I}_{4\alpha,\psi}^{*} - 1\right)^2\right) \tag{37}$$

$$\nu_{\alpha,\psi} = \overline{I}_{4\alpha,\psi}^{*} - \frac{C_1}{2C_2\zeta_{\alpha,\psi}}\left(\exp\left(C_2\left(\overline{I}_{4\alpha,\psi}^{*} - 1\right)^2\right) - 1\right) \tag{38}$$

The ECM free energy W_{ECM} is given by as a function of the first stretch invariant $\overline{I}_1 = \mathrm{tr}\left(\mathbf{C}_{mech}\right)$ of the right Cauchy-Green deformation $\mathbf{C}_{mech} = \mathbf{F}_{mech}^{T}.\mathbf{F}_{mech}$:

$$W_{ECM} = \frac{1}{2}G_{ECM}\left(\overline{I}_1 - 3\right) \tag{39}$$

in which G_{ECM} is the ECM shear modulus.

The chemical free energy W_{chem} is expressed as follows:

$$W_{chem} = \phi_{fluid}\frac{1}{2}\frac{K_1}{K_2}\left(\exp\left(K_2\varepsilon_{chem}^{2}\right) - 1\right) \tag{40}$$

where K_1 and K_2 are material constants, K_1 and K_1/K_2 being the initial and maximal volumetric stiffness values.

The overall Cauchy stress tensor $\boldsymbol{\sigma}_{annulus}$ in the annulus may be calculated as:

$$\boldsymbol{\sigma}_{annulus} = \sum_{i=1,3,..}^{n}\phi_{ring}^{i}\left(\boldsymbol{\sigma}_{mech}^{LM\_i} + \boldsymbol{\sigma}_{chem}^{LM\_i}\right) + \sum_{i=2,4,..}^{n-1}\phi_{ring}^{i}\left(\boldsymbol{\sigma}_{mech}^{ILM\_i} + \boldsymbol{\sigma}_{chem}^{ILM\_i}\right) \tag{41}$$

in which ϕ_{ring}^{i} is the current volume fraction of a ring i:

$$\phi_{ring}^{i} = \frac{\left(\varepsilon_{chem}^{i} + 1\right) t_i}{\sum_{j=1}^{n} \left(\varepsilon_{chem}^{j} + 1\right) t_j} \tag{42}$$

The stress in the nucleus is given by Eq. (15).

2.5.2. Damaged components

The above free energies may be modified to consider the internal stiffness degradation due to the development of mechanical-induced damage [32]:

$$W_{mech} = \left(1 - d_\alpha\right) \phi_{OCF} W_\alpha + \sum_{\psi} \left(1 - d_\psi\right) \phi_\psi W_\psi + \left(1 - d_{ECM}\right) \phi_{ECM} W_{ECM} \tag{43}$$

in which d_α and d_ψ are variables representing the damage events occurring within the interpenetrating collagen fibrillar networks and d_{ECM} is the variable representing the ECM damage.

A continuous damage evolution is assumed over the entire loading history without healing possibilities. The progressive damage of each individual solid component (OCF, NEF and ECM) follows a two-parameter Weibull statistical distribution governed by their respective internal stress:

$$d_\alpha = 1 - \exp\left(-\left(\frac{\left\| \mathbf{P}_{OCF} \right\|}{\beta_{OCF}} \right)^{\gamma_{OCF}} \right) \quad 0 \le d_\alpha \le 1 \tag{44}$$

$$d_\psi = 1 - \exp\left(-\left(\frac{\left\| \mathbf{P}_{\psi} \right\|}{\beta_{NEF}} \right)^{\gamma_{NEF}} \right) \quad 0 \le d_\psi \le 1 \tag{45}$$

$$d_{ECM} = 1 - \exp\left(-\left(\frac{\left\| \mathbf{P}_{ECM} \right\|}{\beta_{ECM}} \right)^{\gamma_{ECM}} \right) \quad 0 \le d_{ECM} \le 1 \tag{46}$$

in which γ_{OCF}, β_{OCF}, γ_{NEF}, β_{NEF}, γ_{ECM} and β_{ECM} are damage parameters. The term $\left\| \mathbf{P} \right\| = \sqrt{\mathrm{tr}\left(\mathbf{P} \cdot \mathbf{P}^T \right)}$ denotes the Frobenius norm of the effective first Piola-Kirchhoff stress $\mathbf{P}$.

A strong coupling exists between hydration and mechanical-induced damage [32]. In ordert to consider the latter coupling, the chemical-induced volumetric strain ε_{chem} in the free energy (40) is affected by the local damage events using the following expression [32]:

$$\varepsilon_{chem} = \left(\det\left(\mathbf{F}_{chem} \right) - 1 \right) \left(1 - d_\alpha\right) \left(1 - \frac{1}{n} \sum_{\psi}^{n} d_\psi \right) \left(1 - d_{ECM}\right) \tag{47}$$

2.6. Overall disc response

For a known deformation state, the torsional couple M_t of the whole disc may be expressed as the additional contribution of the annulus and the nucleus $M_t = M_{t\_annulus} + M_{t\_nucleus}$:

$$M_{t\_annulus} = 2\int_0^{\pi}\int_{r_{inner}^1}^{r_{outer}^n} \sigma_{\theta z}^i \left(r^i\right)^2 \mathrm{d}r^i \mathrm{d}\theta \text{ and } M_{t\_nucleus} = 2\int_0^{\pi}\int_0^{r^0} \sigma_{\theta z}^0 \left(r^0\right)^2 \mathrm{d}r^0 \mathrm{d}\theta \quad (48)$$

in which $\sigma_{\theta z}^i$ is the local shear stress component.

For a known deformation state, the axial load $F_{annulus}$ of the annulus may be expressed by:

$$F_{annulus} = 2\int_0^{\pi}\int_{r_{inner}^1}^{r_{outer}^n} \sigma_{zz}^i r^i \, \mathrm{d}r^i \mathrm{d}\theta \quad (49)$$

The axial load F of the disc is obtained from the following formula:

$$F = 2\int_0^{\pi}\int_{r_{inner}^1}^{r_{outer}^n} \left(2\sigma_{zz}^i - \sigma_{\theta\theta}^i - \sigma_{rr}^i\right) r^i \, \mathrm{d}r^i \mathrm{d}\theta \quad (50)$$

in which σ_{zz}^i, $\sigma_{\theta\theta}^i$ and σ_{rr}^i are the axial, circumferential and radial stress components.

3. Results and discussion

The model was entirely coded in MATLAB software. At this step of the model development, predictions on axially/torsionally loaded discs can be analyzed. The simulations were performed at a displacement rate of 0.01 mm/s and a twist rate of 0.1 °/s in order to maintain quasi-static loading conditions. The maximum ranges are changed according to the observed local fields in the disc core either to compare with existing data or to cause damage of the internal components.

3.1. Model inputs

Table 1 provides the anatomical data used as direct inputs for a lumbar disc model geometry taken from cadaver disc images at the L1-L2 level of the Holzapfel et al. [40] work. The annulus size is considered to be approximately 50% of the disc volume [41] and is subdivided into 15 different lamellae that are intercalated with 14 ILM. The base radius R^0 is calibrated from the cadaver disc images of Holzapfel et al. [40] resulting in a ratio between the sagittal and frontal radii of $R_{sagittal}^0 / R_{frontal}^0$ = 0.68 with a frontal radius of $R_{frontal}^0$ = 15 mm. The values of the OCF orientation (with alternating signs between successive lamellae), the collagen

volume fraction and the fluid volume fraction are extracted from previous documented experimental findings [42-44] and are listed in Table 1. The intrinsic material parameters, identified in a previous work [9], are listed in Tables 2 and 3. A linear interpolation is here achieved for the regional dependent fibers parameters using the formulation provided in Appendix B.

3.2. Overall disc response

The overall disc response predicted by our modeling approach is plotted in Figure 5 for lumbar discs loaded in compression and in torsion. The simulated load curve obtained on a healthy disc upon compression are compared in Figure 5a with available load-displacement experimental data taken from the literature [45-47]. As far as we know, these papers are the only ones that provide data on lumbar discs loaded till failure upon a displacement-controlled compression. Note that the exact level in the lumbar spine is not specified in these experimental works and important variabilities may exist regarding the disc health state of donor (age, degeneration…) and the testing protocol (loading conditions, environment…). In this regard, the predicted curve may be considered as acceptable since it falls through the experimental points. Figure 5b presents the comparison of the predicted torsional response to available moment-rotation experimental data taken from the literature [48-49]. As far as we know, the paper of Farfan et al. [48] is the only one that provides data on lumbar discs twisted till failure. It can be observed that the experimental data of Farfan et al. [48] exhibit a wide range of torsional stiffness. Indeed, the authors performed their experiments on both healthy discs (the two data curves with the greatest torsional stiffness) and degraded discs (the two other data curves with the lowest torsional stiffness). Interestingly, the predicted curve is found very close to the experiments reported for the twisted healthy discs.

Whereas the fibrils in LM (inter-fibrillar fibrils) seems to play a minor role on the disc resistance in compression (Figure 5a), they have an influential and decisive role in the disc torsional stiffness (Figure 5b) in reason of the interpenetrating across the torsion load bearing OCF network. Figure 5a emphasizes a more important role of the NEF network in ILM (inter-lamellar fibrils) on the disc compresision stiffness especially at low applied displacements. By contrast, the NEF network in ILM has a weak influence on the torsional stiffness (Figure 5b).

When the damage process is introduced in the model, the prediction underestimates the experimental points in compression as observed in Figure 5c and matches closely to the experimental points in torsion as observed in Figure 5d. When the OCF damage is excluded from the analysis, the overall torsion response corresponds to the healthy disc one whereas the

overall compression response first follows the damaged disc response path and then converges progressively towards the healthy disc response path at higher applied displacements. When the NEF network damage is not taken into consideration (but the OCF damage still present), the overall torsion response is that of the twisted damaged disc (Figure 5d). The overall response in compression is first that of a healthy disc and then it diverges more and more as the applied displacement increases (Figure 5c). The ECM damage has a minor effect on the overall disc resistance; the main role of the ECM is relegated to the regulation of cellular development [50] and osmotic swelling [51].

Figure 5c shows that the model predictions with and without damage bound the experimental data after 1 mm displacement compression. Our modeling approach is based on the identification of the intrinsic properties of individual solid constituents (ECM, NEF and OCF) while considering their mechanical-induced degradation [9]. It is worth noticing that the constitutive model has been identified at the scale of a unit lamella (stretched along the OCF direction) for the four main disc regions (PO, PI, AO and AI) [9]. The deformation-induced damage in structural units seems different to that involved in whole discs, a least in intensity. Indeed, the transition from the macroscale towards the whole disc does not consider the complex interaction between the solid constituents in the different regions. That leads to an overestimation of the damage and to underestimate the overall load-displacement response as shown in Figure 5c. In their stereo-radiographic experimental study in whole discs, Costi et al. [52] reached the same conclusions when they compared their results to the stretchability of the structural units reported by Skaggs et al. [42]. The experimental failure strain values of the structural units were found by Costi et al. [52] lower than those obtained locally inside a whole disc loaded under the extremes of physiological motion. The interactions between the different regions of the disc should play a role for the passage from the structural unit to the whole macrostructure. It is clear that the passage from a scale to another needs some adjustement to consider effective interactions between the different lamellae and even between the different networks by adjusting the damage severity to correct its effect on the overall disc stiffness. The latter statement holds true for the interpenetrating network of fibrils for which identification has been carried out at the scale of multi-layered annulus stretched along the radial direction [32]. The hydration state of the tissue may also affect the failure [53] and the local damage events. A difference in damage-hydration coupling may be thus also another factor to consider.

Figure 6 highlights the influence of the LM/ILM collagen networks on the overall disc response for combined axial/torsion loadings. As far as we know, no experimental data exists

for comparison with our predictions. The disc stiffness is always more important when a compression is applied in reason of the amplification of the nucleus hydrostatic pressure on the annulus and the OCF stretching. When the disc is subjected to a tension with twisting, the NEF network has no influence on the overall load-displacement curve (Figure 6a). Nonetheless, the NEF network in the LM zone has a preponderant influence on the overall moment-rotation response (Figure 6b). When the disc is subjected to a compression with twisting, the NEF network contributes to the overall load-displacement response but plays an even more significant role on the overall moment-rotation response both in the LM and ILM zones (Figure 6b). Figure 7 shows the influence of the different local damage events on the overall disc response for combined axial/torsion loadings. The local response of the NEF network in tension and in compression leads to two distinct damage behaviors both in the overall load-displacement and moment-rotation curves. It can be observed that the compression-twist combination leads to the premature appearance of damage as compared to the separate loading results shown in Figure 5.

The disc horizontal section change is reported in Figure 8 under different loading conditions. The figure points out the important role of the annulus inter-layer fluid transfer. In a compressed disc, the absence of fluid transfer attenuates significantly the bulge in the annulus and increases it in the nucleus. The tension has an inverse effect for the two disc parts. Indeed, the compression state generates a nucleus bulge in turns restrained by the annulus auxetic response induced by the inter-layer fluid transfer.

3.3. Local stress and strain

In this subsection, the Green-Lagrange strain components are firstly analyzed. The predicted radial strains in the core of compressed and twisted healthy discs are compared in Figure 9 with the stereo-radiographic experimental data of Costi et al. [52]. The model results were averaged in different zones and then normalized by the applied displacement or rotation. Note that the Costi et al. [52] data are typical results averaged for the asymmetric values in the right and left sides of the sagittal plane. A weak regional variation is predicted whereas the twist model results are more regional-dependent. Generally, the model provides acceptable predictions for the different annulus regions under both compression and torsion.

For different loading cases of combined axial/torsion loadings, the local strain components can be analyzed in Figures 10 and 11. The strain fields analysis under different mechanical paths allow to identify how the load is transmitted from the nucleus to the different annulus regions. Figure 10 shows the low strain components that appeared under torsion are extremely

amplified when the nucleus is activated by the combined effect of a compression [38]. Anterior-posterior height difference induces an axial strain gradient in the compressed disc with the lowest values in the anterior outer region and the highest values in the posterior inner region. The circumferential behavior of the compressed disc is mainly governed by the nucleus hydrostatic pressure on the annulus and the annulus collagen fibers tensions; the lowest circumferential strain values are observed in the inner regions and the highest ones in the anterior outer and posterior outer regions. The shear strain component, often related to damage and tears especially in ILM [10, 52, 54], show higher values when the disc is twisted. The locations of the highest shear strains are identified in the outer posterolateral regions.

Figure 11 highlights the very low radial strains upon pure torsion and important values when the compression is applied. In the latter case, which reflects the real loading condition applied to the human disc quasi-permanently compressed by body load, the ILM is found to severly swell whereas the LM shrinks. This phenomenon is different from a disc region to another and leads to an auxetic behavior in the radial direction [39, 55-56]. This volumetric feature of the lamellar structure is fundamental for the disc functionality for maintaining nucleus swelling and absorbing applied loads. It may lead also to an increasing risk of disc delamination and failure propagation in the radial direction of the disc [32]. Interestingly, the auxetic response is also influenced by the disc morphology as evidenced in Figure 12 in which the contour plots of a simplified disc version are presented. The symmetric fields affect the validity and the reality of the local response. Actually, the heterogeneity of the strain fields is determined by the local structure-mechanics relations but also by the morphology in terms of macrostructure and non-symmetric dimensions.

The local stress variation is provided in Figure 13 in the form of the effective stress averaged in the different disc regions. The stresses in the LM zones are strongly regional dependent. The ILM stresses are more or less uniform when a compression state is applied whereas they become strongly heterogeneous in tension. Whatever the loading condition considered, the absence of volumetric effect in the ILM zones generates no bulge along with negligible stresses. The LM zones in the different regions do not behave in the same way vis-à-vis their dependence on the fluid transfer. Indeed, without the fluid transfer process, the anterior, anterior-lateral and lateral regions have a significant increase of the stresses whereas they decrease in the posterior-lateral and posterior regions.

3.4. Damage fields

In this subsection, the deformation-induced damage fields are analyzed for the different solid components (ECM, NEF and OCF) in order to identify their respective role in the starting areas of failure modes under combined axial/torsion loadings. Recall that the damage intensity is somewhat magnified in regards to the comparison to the overall response and to the issue of the passage from the structural unit to the whole macrostructure. Nonetheless, the location of damage maxima remains valid and may be related to existing disc damage mechanisms experimentally reported for whole discs in [29-31].

The ECM and NEF damage are presented both in LM and in ILM in Figures 14 and 15, respectively. The ECM and the network of inter-lamellar fibrils (in LM) of the anterior side are more likely damaged when the disc is compressed. The latter can be the sign of the starting areas of the annulus delamination failure mode. The nucleus-annulus interface is also the site of a damage zone (Figures 14b and 15b) due to the pressure difference between the two portions, suggesting increasing the possibility of tear creation in the interface. When the disc is stretched, the highest damage zones are shifted from the anterior side to the posterior side. Compared to the NEF network in ILM, the damage of inter-fibrillar fibrils (in LM) exhibits a very low intensity with an important effect of the loading mode both for the intensity and the extent. Whatever the loading mode, the highest ECM damage zones in LM are located in the posterior side.

Figure 16 shows the loading mode has a profound effect on the OCF damage. When the disc is compressed the highest OCF damage zones are mainly observed in mid-anterior/lateral anterior ring. The latter can be the sign of the starting areas of annulus circumferential tears. Combined to a compression, the twisted disc presents the highest OCF damage zones for the fibers oriented in the twist direction with a progression from the AO side to the PO side. The alternate fibers are only damaged in a small area of the AO side. When the twisted disc is combined to a tension, the damage progression is reversed from the posterior side to the anterior side and, the damage of the alternate fibers is located in the PO region. The NEF network in ILM follows the same reverse compression/tension effect as shown in Figure 16. The latter may be due to the nucleus swelling effect but also to the anterior-posterior height difference.

4. Conclusion

In this work, we have presented a new and direct analytical method for the creation of human discs considering accurate morphology, multiscale structure (ECM proteoglycan macromolecules, interpenetrating collagen fibrillar networks and LM/ILM/nucleus

interaction) and coupled damage-hydration effects. A first quantitative evaluation of the disc model was presented using available experimental observations of the literature. The model was favorably compared with compression/torsion experiments both for the overall disc stiffness and for the direct MRI kinematic fields. The model was then used to assess the local fields under combined axial/torsion loadings and especially the damage areas where the risk of failure is the highest. Our new approach provides an accurate microstructure-mechanics relationship of the human disc while providing versatile possibilities of regional-dependent geometry variations, the final goal being to create time and cost-efficient patient-specific models.

In the future, the patient-specific models using our new approach need verifications with in vivo clinical MRI images. In the meantime, although quite sophisticated, the present model needs improvements. The model can be improved by acting on the constitutive representation to take into consideration the biological coupling in order to assess the long-term biomechanical damage effects inside the disc induced by physiological activity and age. In this regards, other physiological movements (e.g. flexion/extension) could be introduced in further developments of the disc kinematics in order propose quantitative predictions of the disc health and functionality under more complex loading modes.

Acknowledgements

This work was financially supported by the PROFAS B+ Scholarships Program and the International Mobility Grants Program of the University of Lille.

Appendix A. Structure regional variation

A.1. OCF regional variation

The regional variation in OCF angle is taken into account using the following linear equation:

$$\alpha_0^i = a^- i + b^- \text{ for } i = 3,7,11...n \tag{A1}$$

$$\alpha_0^i = a^+ i + b^+ \text{ for } i = 1,5,9...n-2 \tag{A2}$$

with

$$a^{+/-} = \frac{\left(\alpha_{PO}^{+/-} + \alpha_{AI}^{+/-} - \alpha_{AO}^{+/-} - \alpha_{PI}^{+/-}\right)\Theta + \left(\alpha_{AO}^{+/-} - \alpha_{AI}^{+/-}\right)\pi}{\left(n-1\right)\pi} \tag{A3}$$

$$b^{+/-} = \frac{\left(\alpha_{PI}^{+/-} - \alpha_{AI}^{+/-}\right)\Theta + \alpha_{AI}^{+/-}\pi}{\pi} - a^{+/-} \tag{A4}$$

in which $\alpha_{PO}^{+/-}$, $\alpha_{PI}^{+/-}$, $\alpha_{AO}^{+/-}$ and $\alpha_{AI}^{+/-}$ are the regional OCF angles.

A.2. NEF regional variation

The volume fraction of a fibril in each ring *i* is given by:

$$\phi_{\eta}^{LM\_i}=\begin{cases}\dfrac{q_{\eta}^{LM\_i}+q_{\eta}^{ILM\_i}}{q^{LM\_i}} & \eta=0°,180° \\ \dfrac{q_{\eta}^{LM\_i}}{q^{LM\_i}} & \eta=45°,90°,135°\end{cases} \quad \text{and} \quad \phi_{\eta}^{ILM\_i}=\begin{cases}0 & \eta=0°,180° \\ \dfrac{q_{\eta}^{ILM\_i}}{q^{ILM\_i}} & \eta=45°,90°,135°\end{cases} \tag{A5}$$

where q^{LM_i} and q^{ILM_i} are the respective total number of NEF in each ring *i*:

$$q^{LM\_i}=\sum_{\eta}\sum_{\psi}q_{\eta}^{LM\_i}+\sum_{\eta=0°,180°}\sum_{\psi}q_{\eta}^{ILM\_i} \quad \text{and} \quad q^{ILM\_i}=\sum_{\eta=45°,90°,135°}\sum_{\psi}q_{\eta}^{ILM\_i} \tag{A6}$$

The quantities $q_{\eta}^{LM\_i}$ and $q_{\eta}^{ILM\_i}$ are descibed using Gaussian probability density functions:

$$q_{\eta}^{LM\_i}=\chi_{\eta}^{LM\_i}\exp\left(-\varsigma_{\eta}^{LM\_i}\left(\psi-\eta\right)^2\right) \quad \text{and} \quad q_{\eta}^{ILM\_i}=\chi_{\eta}^{ILM\_i}\exp\left(-\varsigma_{\eta}^{ILM\_i}\left(\psi-\eta\right)^2\right) \tag{A7}$$

where $\chi_{\eta}^{LM\_i}$ and $\chi_{\eta}^{ILM\_i}$ denote the respective peak values of each fibrils bundle η = {0°, 45°, 90°, 135°, 180°} (Figure 4):

$$\chi_{\eta}^{LM\_i}=a_{\chi\_\eta}^{LM}i+b_{\chi\_\eta}^{LM} \quad \text{and} \quad \chi_{\eta}^{ILM\_i}=a_{\chi\_\eta}^{ILM}i+b_{\chi\_\eta}^{ILM} \tag{A8}$$

and, $\varsigma_{\eta}^{LM\_i}$ and $\varsigma_{\eta}^{ILM\_i}$ are unitless scale factors:

$$\varsigma_{\eta}^{LM\_i}=a_{\varsigma\_\eta}^{LM}i+b_{\varsigma\_\eta}^{LM} \text{ and } \varsigma_{\eta}^{ILM\_i}=a_{\varsigma\_\eta}^{ILM}i+b_{\varsigma\_\eta}^{ILM} \tag{A9}$$

The terms $a_{\chi\_\eta}^{LM,ILM}$ and $b_{\chi\_\eta}^{LM,ILM}$ are expressed as a function of the posterior peak values $\chi_{\eta\_PO}^{LM,ILM}$ and $\chi_{\eta\_PI}^{LM,ILM}$ ($\Theta=\pi$) of the outer ring $i=n$ and the anterior peak values $\chi_{\eta\_AO}^{LM,ILM}$ and $\chi_{\eta\_AI}^{LM,ILM}$ ($\Theta=0$) of the inner ring $i=1$:

$$a_{\chi\_\eta}^{LM,ILM}=\frac{\left(\chi_{\eta\_PO}^{LM,ILM}+\chi_{\eta\_AI}^{LM,ILM}-\chi_{\eta\_AO}^{LM,ILM}-\chi_{\eta\_PI}^{LM,ILM}\right)\Theta+\left(\chi_{\eta\_AO}^{LM,ILM}-\chi_{\eta\_AI}^{LM,ILM}\right)\pi}{\left(n-1\right)\pi} \tag{A10}$$

$$b_{\chi\_\eta}^{LM,ILM}=\frac{\left(\chi_{\eta\_PI}^{LM,ILM}-\chi_{\eta\_AI}^{LM,ILM}\right)\Theta+\chi_{\eta\_AI}^{LM,ILM}\pi}{\pi}-a_{\chi\_\eta}^{LM,ILM} \tag{A11}$$

The terms $a_{\varsigma\_\eta}^{LM,ILM}$ and $b_{\varsigma\_\eta}^{LM,ILM}$ are expressed as a function of the posterior and anterior scale factors $\varsigma_{\eta\_PO}^{LM,ILM}$, $\varsigma_{\eta\_PI}^{LM,ILM}$, $\varsigma_{\eta\_AO}^{LM,ILM}$ and $\varsigma_{\eta\_AI}^{LM,ILM}$:

$$a_{\varsigma\_\eta}^{LM,ILM}=\frac{\left(\varsigma_{\eta\_PO}^{LM,ILM}+\varsigma_{\eta\_AI}^{LM,ILM}-\varsigma_{\eta\_AO}^{LM,ILM}-\varsigma_{\eta\_PI}^{LM,ILM}\right)\Theta+\left(\varsigma_{\eta\_AO}^{LM,ILM}-\varsigma_{\eta\_AI}^{LM,ILM}\right)\pi}{\left(n-1\right)\pi} \tag{A12}$$

$$b_{\varsigma\_\eta}^{LM,ILM} = \frac{\left(\varsigma_{\eta\_PI}^{LM,ILM} - \varsigma_{\eta\_AI}^{LM,ILM}\right)\Theta + \varsigma_{\eta\_AI}^{LM,ILM}\pi}{\pi} - a_{\varsigma\_\eta}^{LM,ILM} \tag{A13}$$

Appendix B. Material properties regional variation

The OCF parameters were identified in our previous work [9] on the different annulus regions. The regional variation is taken into account using a simple linear interpolation according to the following equation:

$$C^i = a_C i + b_C \tag{B1}$$

with

$$a_C = \frac{\left(C_{PO} + C_{AI} - C_{AO} - C_{PI}\right)\Theta + \left(C_{AO} - C_{AI}\right)\pi}{\left(n-1\right)\pi} \tag{B2}$$

$$b_C = \frac{\left(C_{PI} - C_{AI}\right)\Theta + C_{AI}\pi}{\pi} - a_C \tag{B3}$$

in which C_{PO}, C_{PI}, C_{AO} and C_{AI} are the regional material properties given in Table 3.

References

[1] Asner, L., Hadjicharalambous, M., Chabiniok, R., Peressutti, D., Sammut, E., Wong, J., Carr-White, G., Razavi, R., King, A., Smith, N., Lee, J., Nordsletten, D., 2017. Patient-specific modeling for left ventricular mechanics using data-driven boundary energies. Computer Methods in Applied Mechanics and Engineering 314, 269-295.

[2] Rama, R.R., Skatulla, S., 2018. Towards real-time cardiac mechanics modelling with patient-specific heart anatomies. Computer Methods in Applied Mechanics and Engineering 328, 47-74.

[3] Lauzeral, N., Borzacchiello, D., Kugler, M., George, D., Rémond, Y., Hostettler, A., Chinesta, F., 2019. A model order reduction approach to create patient-specific mechanical models of human liver in computational medicine applications. Computer Methods and Programs in Biomedicine 170, 95-106.

[4] Razaghi, R., Biglari, H., Karimi, A., 2019. Risk of rupture of the cerebral aneurysm in relation to traumatic brain injury using a patient-specific fluid-structure interaction model. Computer Methods and Programs in Biomedicine 176, 9-16.

[5] Grytz, R., Krishnan, K., Whitley, R., Libertiaux, V., Sigal, I.A., Girkin, C.A., Downs J.C., 2020. A mesh-free approach to incorporate complex anisotropic heterogeneous material properties into eye-specific finite element models. Computer Methods in Applied Mechanics and Engineering 358, 112654.

[6] Tavakoli, J., Diwan, A.D., Tipper, J.L., 2020. The ultrastructural organization of elastic fibers at the interface of the nucleus and annulus of the intervertebral disk. Acta Biomaterialia 114, 323-332.

[7] Tavakoli, J., Diwan, A.D., Tipper, J.L., 2020. Elastic fibers: the missing key to improve engineering concepts for reconstruction of the nucleus pulposus in the intervertebral disc. Acta Biomaterialia 113, 407-416.

[8] Kandil, K., Zaïri, F., Messager, T., Zaïri, F., 2020. Interlamellar matrix governs human annulus fibrosus multiaxial behavior. Scientific Reports 10, 19292.

[9] Tamoud, A., Zaïri, F., Mesbah, A., Zaïri, F., 2021. Modeling multiaxial damage regional variation in human annulus fibrosus. Acta Biomaterialia 136, 375-388.
[10] Goel, V.K., Monroe, B.T., Gilbertson, L.G., Brinckmann, P., 1995. Interlaminar shear stresses and laminae separation in a disc. Finite element analysis of the L3-L4 motion segment subjected to axial compressive loads. Spine 20, 689-698.
[11] Qasim, M., Natarajan, R.N., An, H.S., Andersson, G.B.J., 2012. Initiation and progression of mechanical damage in the intervertebral disc under cyclic loading using continuum damage mechanics methodology: a finite element study. Journal of Biomechanics 45, 1934-1940.
[12] Qasim, M., Natarajan, R.N., An, H.S., Andersson, G.B.J., 2014. Damage accumulation location under cyclic loading in the lumbar disc shifts from inner annulus lamellae to peripheral annulus with increasing disc degeneration. Journal of Biomechanics 47, 24-31.
[13] Shahraki, N.M., Fatemi, A., Agarwal, A., Goel, V.K., 2015. Failure criteria for prediction of clinically relevant damage of annulus fibrosus. Spine Research 1, 7.
[14] Masni, A., Tanaka, M., 2018. Biomechanical investigation on the influence of the regional material degeneration of an intervertebral disc in a lower lumbar spinal unit: a finite element study. Computers in Biology and Medicine 98, 26-38.
[15] Stadelmann, M.A., Maquer, G., Voumard, B., Grant, A., Hackney, D.B., Vermathen, P., Alkalay, R.V., Zysset, P. K., 2018. Integrating MRI-based geometry, composition and fiber architecture in a finite element model of the human intervertebral disc. Journal of the Mechanical Behavior of Biomedical Materials 85, 37-42.
[16] Disney, C.M., Eckersley, A., McConnell, J.C., Geng, H., Bodey, A.J., Hoyland, J.A., Lee, P.D., Sherratt, M.J., Bay, B.K., 2019. Synchrotron tomography of intervertebral disc deformation quantified by digital volume correlation reveals microstructural influence on strain patterns. Acta Biomaterialia 92, 290-304.
[17] Castro, A.P.G., Alves, J.L., 2020. Numerical implementation of an osmo-poro-visco-hyperelastic finite element solver: application to the intervertebral disc. Computer Methods in Biomechanics and Biomedical Engineering 5, 538-550.
[18] Subramani, A.V., Whitley, P.E., Garimella, H.T., Kraft, R.H., 2020. Fatigue damage prediction in the annulus of cervical spine intervertebral discs using finite element analysis. Computer Methods in Biomechanics and Biomedical Engineering 23, 773-784.
[19] Yoon, D.H.E., Weber, C.I., Easson, G.W., Broz, K.S., Tang, S.Y., 2020. Rapid determination of internal strains in soft tissues using an experimentally calibrated finite element model derived from magnetic resonance imaging. Quantitative Imaging in Medicine and Surgery 10, 57-65.
[20] Du, Y., Tavana, S., Rahman, T., Baxan, N., Hansen, U.N., Newell, N., 2021. Sensitivity of intervertebral disc finite element models to internal geometric and non-geometric parameters. Frontiers in Bioengineering and Biotechnology 9, 509.
[21] Mengoni, M., Zapata-Cornelio, F.Y., Wijayathunga, V.N., Wilcox, R.K., 2021. Experimental and computational comparison of intervertebral disc bulge for specimen-specific model evaluation based on imaging. Frontiers in Bioengineering and Biotechnology 9, 661469.
[22] Kandil, K., Zaïri, F., Messager, T., Zaïri, F., 2021. A microstructure-based model for a full lamellar-interlamellar displacement and shear strain mapping inside human intervertebral disc core. Computers in Biology and Medicine 135, 104629.
[23] Komeili, A., Rasoulian, A., Moghaddam, F., El-Rich, M., 2021. The importance of intervertebral disc material model on the prediction of mechanical function of the cervical spine. BMC Musculoskeletal Disorders 22, 1-12.
[24] Amonoo-Kuofi, H.S., 1991. Morphometric changes in the heights and anteroposterior diameters of the lumbar intervertebral discs with age. Journal of Anatomy 175, 159-168.

[25] Kim, K.H., Park, J.Y., Kuh, S.U., Chin, D.K., Kim, K.S., Cho, Y.E., 2013. Changes in spinal canal diameter and vertebral body height with age. Yonsei Medical Journal 54, 1498-1504.
[26] Kandil, K., Zaïri, F., Messager, T., Zaïri, F., 2021. A microstructure-based mechanistic modeling approach to assess aging-sensitive response of human intervertebral disc. Computer Methods and Programs in Biomedicine, 105890.
[27] Urban, J.P., Maroudas, A., 1981. Swelling of the intervertebral disc in vitro. Connective Tissue Research 9, 1-10.
[28] Derrouiche, A., Zaouali, A., Zaïri, F., Ismail, J., Chaabane, M., Qu, Z., Zaïri, F., 2019. Osmo-inelastic response of the intervertebral disc. Proceedings of the Institution of Mechanical Engineers. Part H: Journal of Engineering in Medicine 233, 332-341.
[29] Osti, O.L., Vernon-Roberts, B., Moore, R., Fraser, R.D., 1992. Annular tears and disc degeneration in the lumbar spine: a post-mortem study of 135 discs. The Journal of Bone and Joint Surgery 74, 678-682.
[30] Schollum, M.L., Robertson, P.A., Broom, N.D., 2008. ISSLS prize winner: microstructure and mechanical disruption of the lumbar disc annulus: part I: a microscopic investigation of the translamellar bridging network. Spine 33, 2702-2710.
[31] Sapiee, N.H., Thambyah, A., Robertson, P.A., Broom, N.D., 2019. Sagittal alignment with downward slope of the lower lumbar motion segment influences its modes of failure in direct compression: A mechanical and microstructural investigation. Spine 44, 1118-1128.
[32] Tamoud, A., Zaïri, F., Mesbah, A., Zaïri, F., 2021. A multiscale and multiaxial model for anisotropic damage and failure of human annulus fibrosus. International Journal of Mechanical Sciences 205, 106558.
[33] Ogden, R.W., 1997. Non-linear elastic deformations. Dover Publication, New York.
[34] Kanner, L.M., Horgan, C.O., 2008. On extension and torsion of strain-stiffening rubber-like elastic circular cylinders. Journal of Elasticity 93, 39-61.
[35] Horgan, C.O., Murphy, J.G., 2011. Extension and torsion of incompressible non-linearly elastic solid circular cylinders. Mathematics and Mechanics of Solids. 16, 482-491.
[36] Holzapfel, G.A., Gasser, T.C., Ogden, R.W., 2000. A new constitutive framework for arterial wall mechanics and a comparative study of material models. Journal of Elasticity and the Physical Science of Solids 61, 1-48.
[37] Shah, J.S., Hampson, W.G., Jayson, M.I., 1978. The distribution of surface strain in the cadaveric lumbar spine. Journal of Bone and Joint Surgery 60, 246-251.
[38] Derrouiche, A., Feki, F., Zaïri, F., Taktak, R., Moulart, M., Qu, Z., Ismail, J., Charfi, S., Haddar, N., Zaïri, F., 2020. How pre-strain affects the chemo-torsional response of the intervertebral disc. Clinical Biomechanics 76, 105020.
[39] Tamoud, A., Zaïri, F., Mesbah, A., Zaïri, F., 2021. A microstructure-based model for time-dependent mechanics of multi-layered soft tissues and its application to intervertebral disc annulus. Meccanica 56, 585-606.
[40] Holzapfel, G.A., Schulze-Bauer, C.A., Feigl, G., Regitnig, P., 2005. Single lamellar mechanics of the human lumbar anulus fibrosus. Biomechanics and Modeling in Mechanobiology 3, 125-140.
[41] Violas, P., Estivalezes, E., Briot, J., Sales de Gauzy, J., Swider P., 2007. Objective quantification of intervertebral disc volume properties using MRI in idiopathic scoliosis surgery. Magnetic Resonance Imaging 25, 386-391.
[42] Skaggs, D.L., Weidenbaum, M., Iatridis, J.C., Ratcliffe, A., Mow, V.C., 1994. Regional variation in tensile properties and biochemical composition of the human lumbar anulus fibrosus. Spine 19, 1310-1319.

[43] Acaroglu, E.R., Iatridis, J.C., Setton, L.A., Foster, R.J., Mow, V.C., Weidenbaum, M., 1995. Degeneration and aging affect the tensile behavior of human lumbar anulus fibrosus. Spine 20, 2690-2701.
[44] Ebara, S., Iatridis, J.C., Setton, L.A., Foster, R.J., Mow, V.C., Weidenbaum, M., 1996. Tensile properties of nondegenerate human lumbar anulus fibrosus. Spine 21, 452-461.
[45] Virgin, W.J., 1951. Experimental investigations into the physical properties of the intervertebral disc. The Journal of Bone and Joint Surgery 33, 607-611.
[46] Markolf, K.L., Morris, J.M., 1974. The structural components of the intervertebral disc: a study of their contributions to the ability of the disc to withstand compressive forces. The Journal of Bone and Joint Surgery 56, 675-687.
[47] Adams, M.A., McNally, D.S., Wagstaff, J., Goodship, A.E., 1993. Abnormal stress concentrations in lumbar intervertebral discs following damage to the vertebral bodies: a cause of disc failure? European Spine Journal 1, 214-221.
[48] Farfan, H. F., Cossette, J. W., Robertson, G. H., Wells, R. V., Kraus, H.T., 1970. The effects of torsion on the lumbar intervertebral joints: the role of torsion in the production of disc degeneration. The Journal of Bone & Joint Surgery 52, 468-497.
[49] Markolf, K.L., 1972. Deformation of the thoracolumbar intervertebral joints in response to external loads: a biomechanical study using autopsy material. The Journal of Bone & Joint Surgery 54, 511-533.
[50] Melrose, J., Ghosh, P., Taylor, T.K., 2001. A comparative analysis of the differential spatial and temporal distributions of the large (aggrecan, versican) and small (decorin, biglycan, fibromodulin) proteoglycans of the intervertebral disc. The Journal of Anatomy 198, 3-15.
[51] Feki, F., Taktak, R., Kandil, K., Derrouiche, A., Moulart, M., Haddar, N., Zaïri, F., Zaïri, F., 2020. How osmoviscoelastic coupling affects recovery of cyclically compressed intervertebral disc. Spine 45, E1376-E1385.
[52] Costi, J.J., Stokes, I.A., Gardner-Morse, M., Laible, J.P., Scoffone, H.M., Iatridis, J.C., 2007. Direct measurement of intervertebral disc maximum shear strain in six degrees of freedom: motions that place disc tissue at risk of injury. Journal of Biomechanics 40, 2457-2466.
[53] Werbner, B., Spack, K., O'Connell, G.D., 2019. Bovine annulus fibrosus hydration affects rate-dependent failure mechanics in tension. Journal of Biomechanics 89, 34-39.
[54] Iatridis, J.C., ap Gwynn, I., 2004. Mechanisms for mechanical damage in the intervertebral disc annulus fibrosus. Journal of Biomechanics 37, 1165-1175.
[55] Derrouiche, A., Zaïri, F., Zaïri, F., 2019. A chemo-mechanical model for osmo-inelastic effects in the annulus fibrosus. Biomechanics and Modeling in Mechanobiology 18, 1773-1790.
[56] Kandil, K., Zaïri, F., Derrouiche, A., Messager, T., Zaïri, F., 2019. Interlamellar-induced time-dependent response of disc annulus: a microstructure-based chemo-viscoelastic model. Acta Biomaterialia 100, 75-91.

	Regions				References
	AO	AI	PO	PI	
Layer thickness [mm]	t_{AO}	t_{AI}	t_{PO}	t_{PI}	[40]
	0.69	0.76	0.38	0.40	
Disc height [mm]	H_{AO}	H_{AI}	H_{PO}	H_{PI}	[40]
	12.8	8.40	8.00	7.20	
OCF orientation [deg]	$\alpha_{AO}^{+/-}$	$\alpha_{AI}^{+/-}$	$\alpha_{PO}^{+/-}$	$\alpha_{PI}^{+/-}$	[40]
	+25.7/-22.1	+29.9/-27.6	+49.3/-50.1	+45.8/-46.1	
Collagen volume fraction [-]	ϕ_{coll_AO}	ϕ_{coll_AI}	ϕ_{coll_PO}	ϕ_{coll_PI}	[42]
	0.127	0.087	0.135	0.093	
Fluid volume fraction [-]	ϕ_{fluid_AO}	ϕ_{fluid_AI}	ϕ_{fluid_PO}	ϕ_{fluid_PI}	[43-44]
	0.710	0.790	0.695	0.800	

Table 1. Disc macrostructure and structure features.

Constituents	Parameters		
ECM	G_{ECM}	[MPa]	0.01
	γ_{ECM}	[-]	2
	β_{ECM}	[MPa]	5.5
NEF	C_1	[MPa]	12
	C_2	[-]	0.2
	C_3	[MPa]	1.5
	λ_{ψ}^{*}	[-]	1.7
	γ_{NEF}	[-]	6
	β_{NEF}	[MPa]	400
Swelling	K_1	[MPa]	0.14
	K_2	[-]	0.0075

Table 2. ECM, NEF and swelling parameters [9].

Parameters		Regions			
		AO	PO	AI	PI
C_1	[MPa]	40	26	26	3
C_2	[-]	880	58	30	11
C_3	[MPa]	500	300	400	80
λ_{θ}^{*}	[-]	1.02	1.07	1.1	1.14
γ_{OCF}	[-]	5	5	5	5
β_{OCF}	[MPa]	215	125	120	70

Table 3. OCF parameters [9].

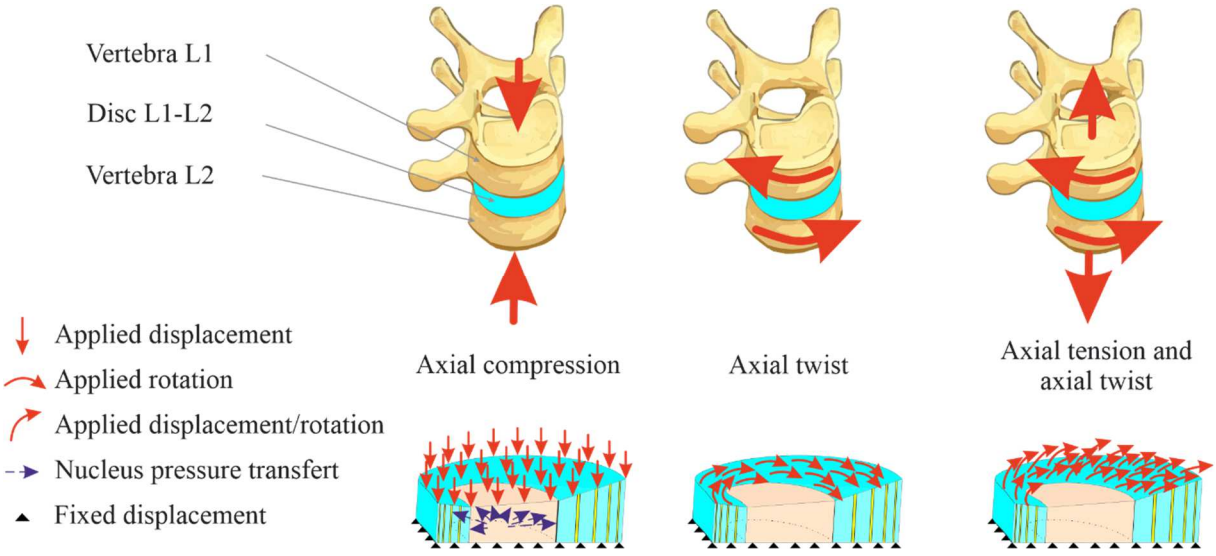

Figure 1. Axially/torsionally loaded functional spine unit (i.e. an intervertebral disc and two adjacent vertebrae) and related boundary conditions on the disc.

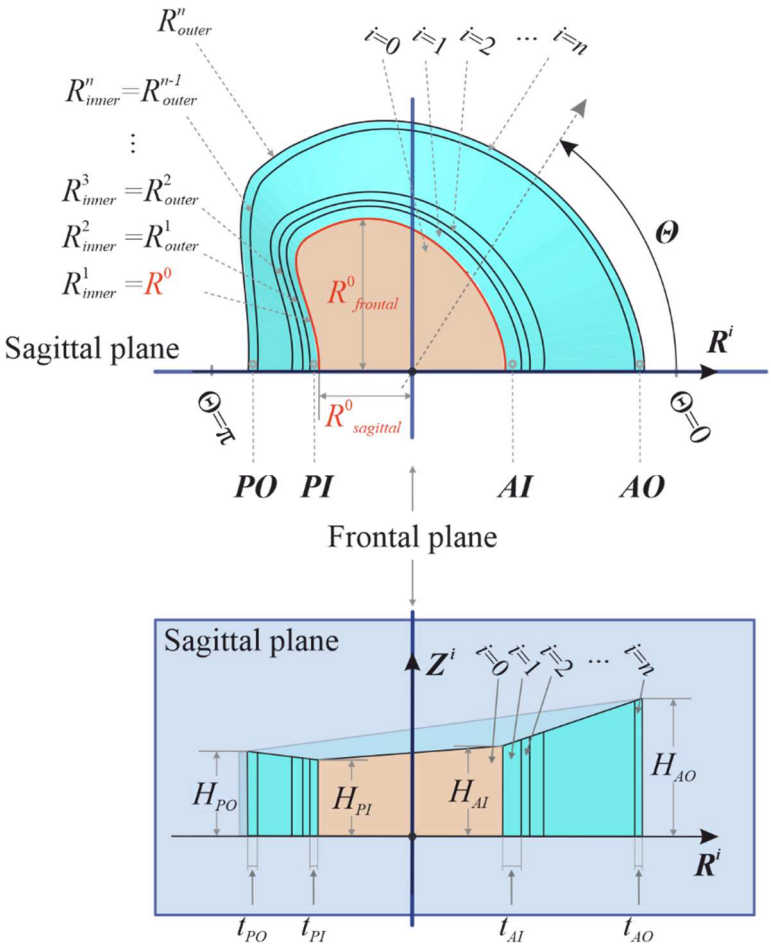

Figure 2. Disc macrostructure in the polar coordinates.

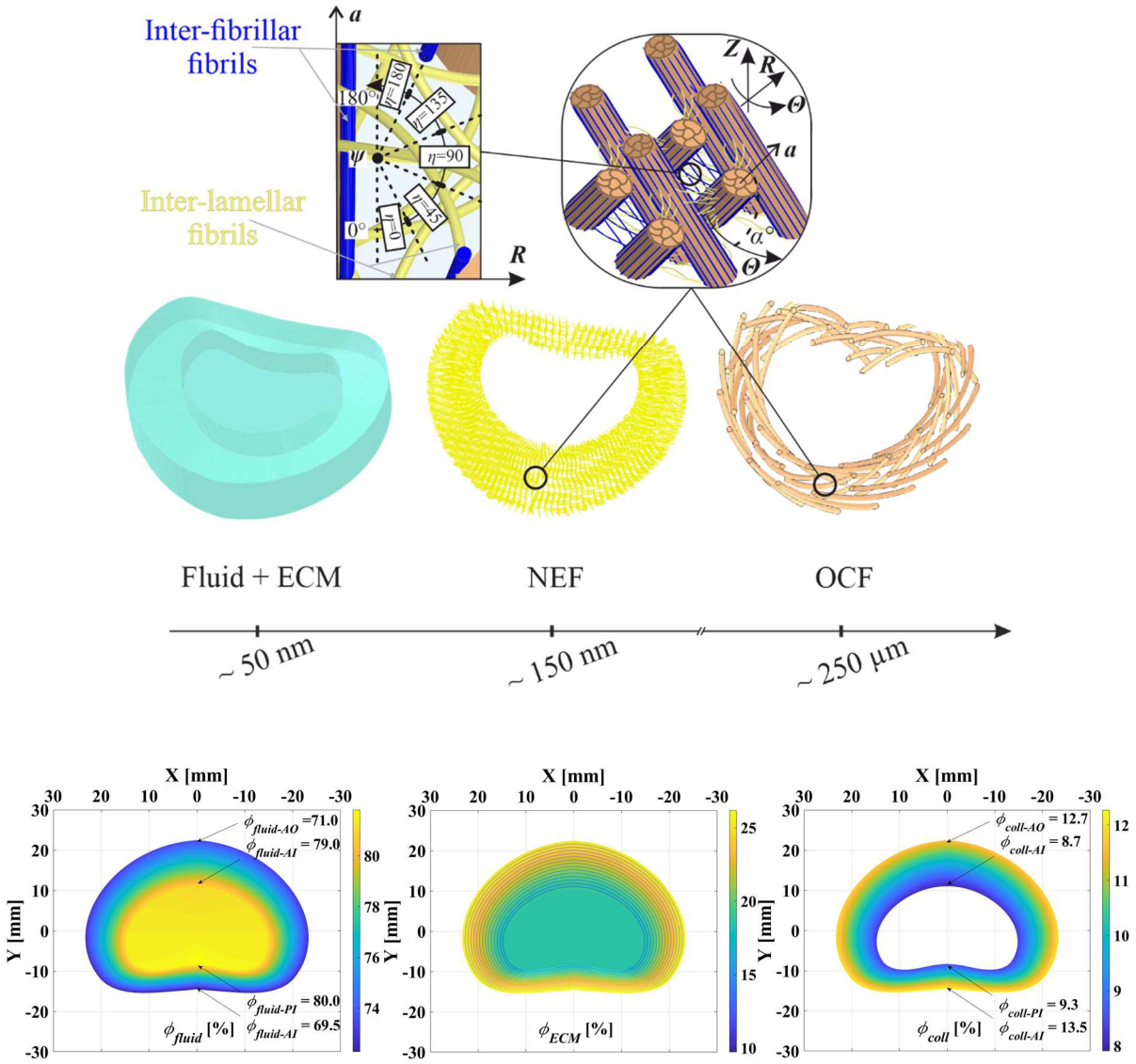

Figure 3. Disc structure decomposition into ECM (along with fluid) and interpenetrating collagen fibrillar networks at the nanoscale (NEF) and at the microscale (OCF). Contour plots in the superior view of the disc show the regional dependent quantities in terms of fluid phase fraction ϕ_{fluid}, collagen fraction $\phi_{coll} = \phi_{NEF} + \phi_{OCF}$ and ECM fraction $\phi_{ECM} = 1 - \phi_{fluid} - \phi_{coll}$.

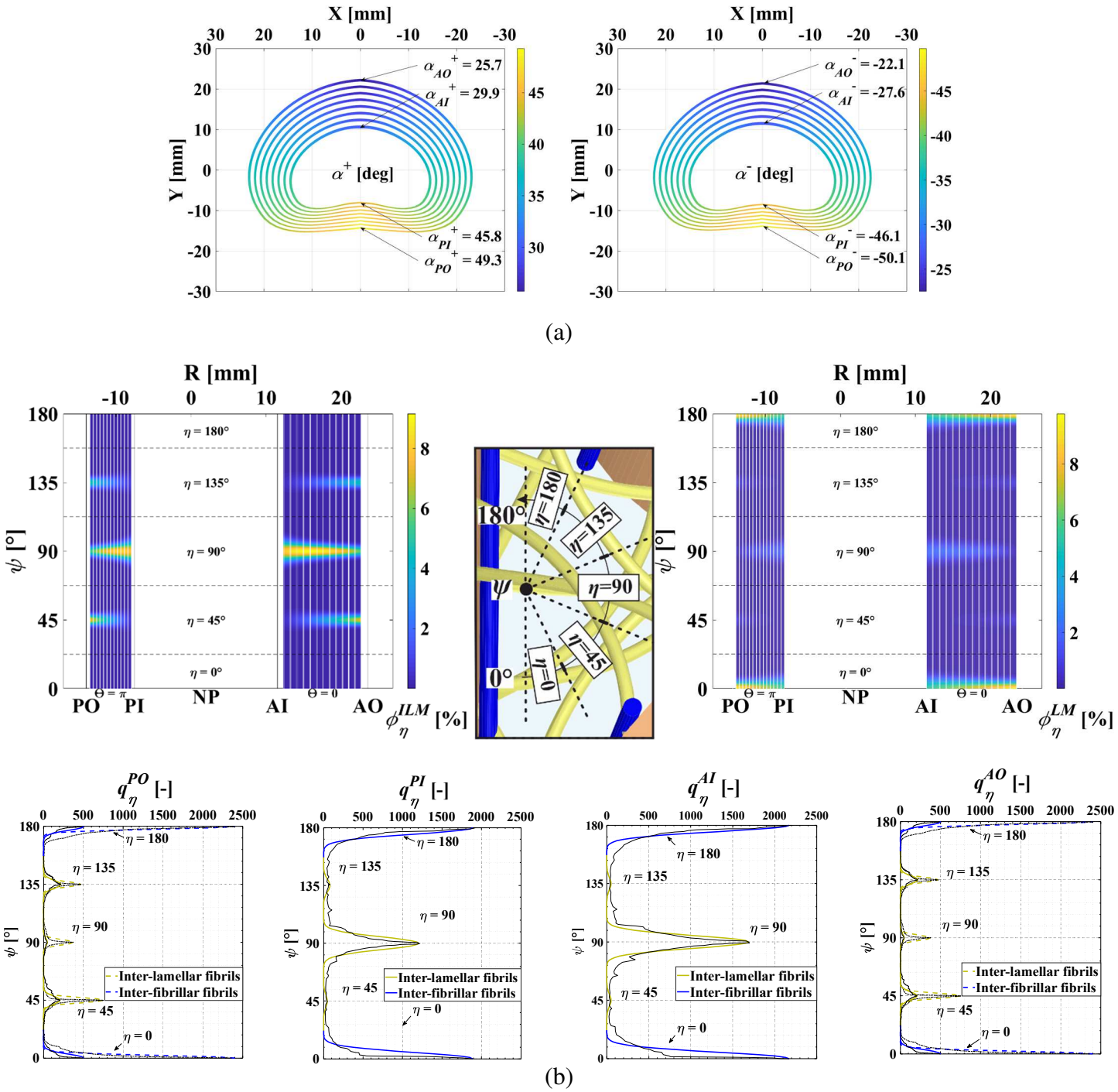

Figure 4. Organization of the interpenetrating collagen fibrillar networks: (a) OCF angle in the form of contour plots in the superior view of the disc, (b) fibrils angle in the form of contour plots in the sagittal view of the disc. The fibrils spatial distribution is obtained by the linear interpolation of approximated Gaussian-type distributions in the outer and inner boundaries of PO (Posterior-Outer), AO (Anterior-Outer), PI (Posterior-Inner) and AI (Anterior-Inner) regions. The dashed lines in the Gaussian-type distributions are experimental data extracted from the work of Tavakoli et al. [6-7].

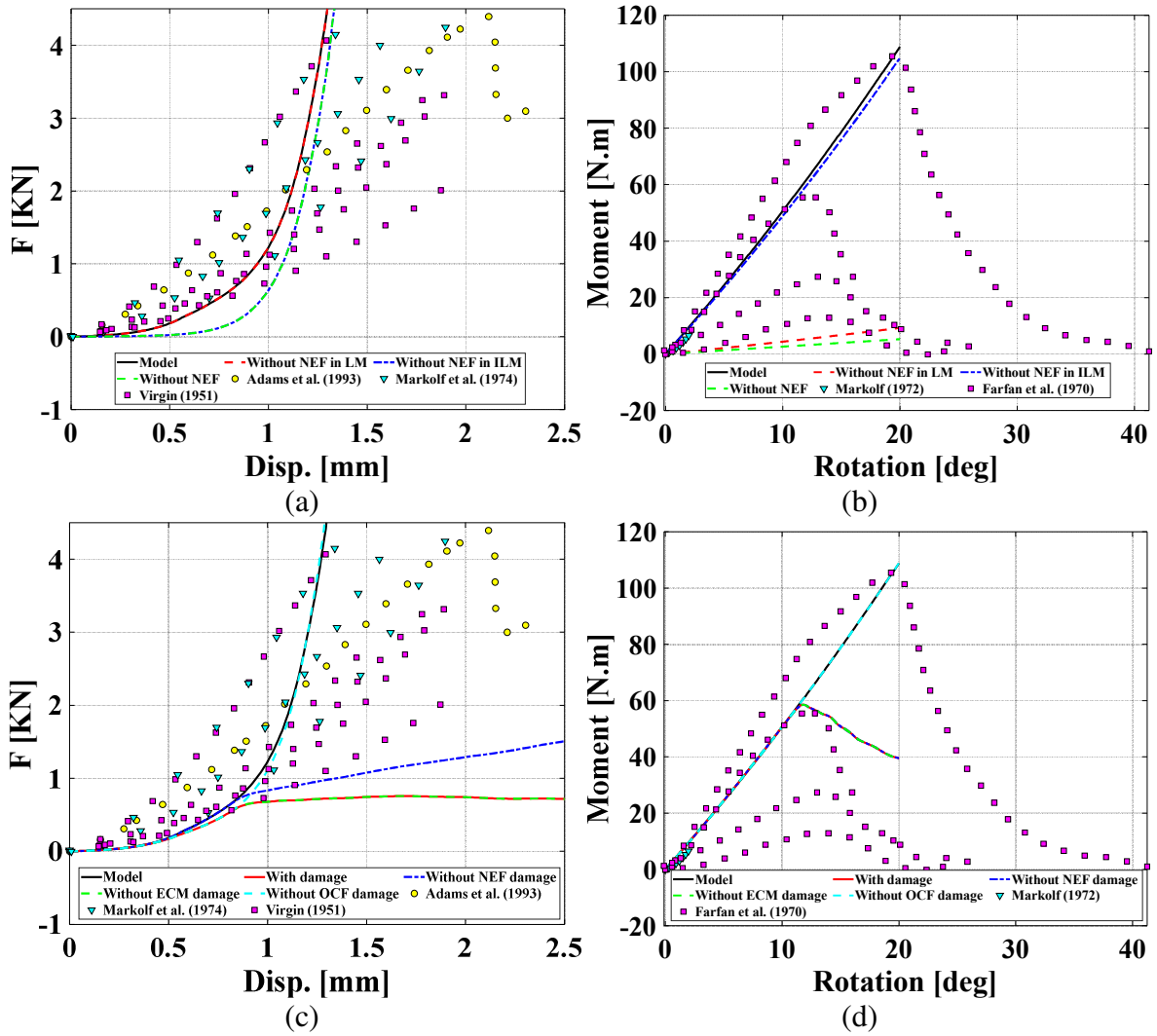

Figure 5. Predicted load curves of the compressed disc and moment curves of the twisted disc in comparison to experiments (lines: model; symbols: experiments): (a) influence of the LM/ILM collagen networks in compression, (b) in torsion, (c) influence of the damage events in compression, (d) in torsion.

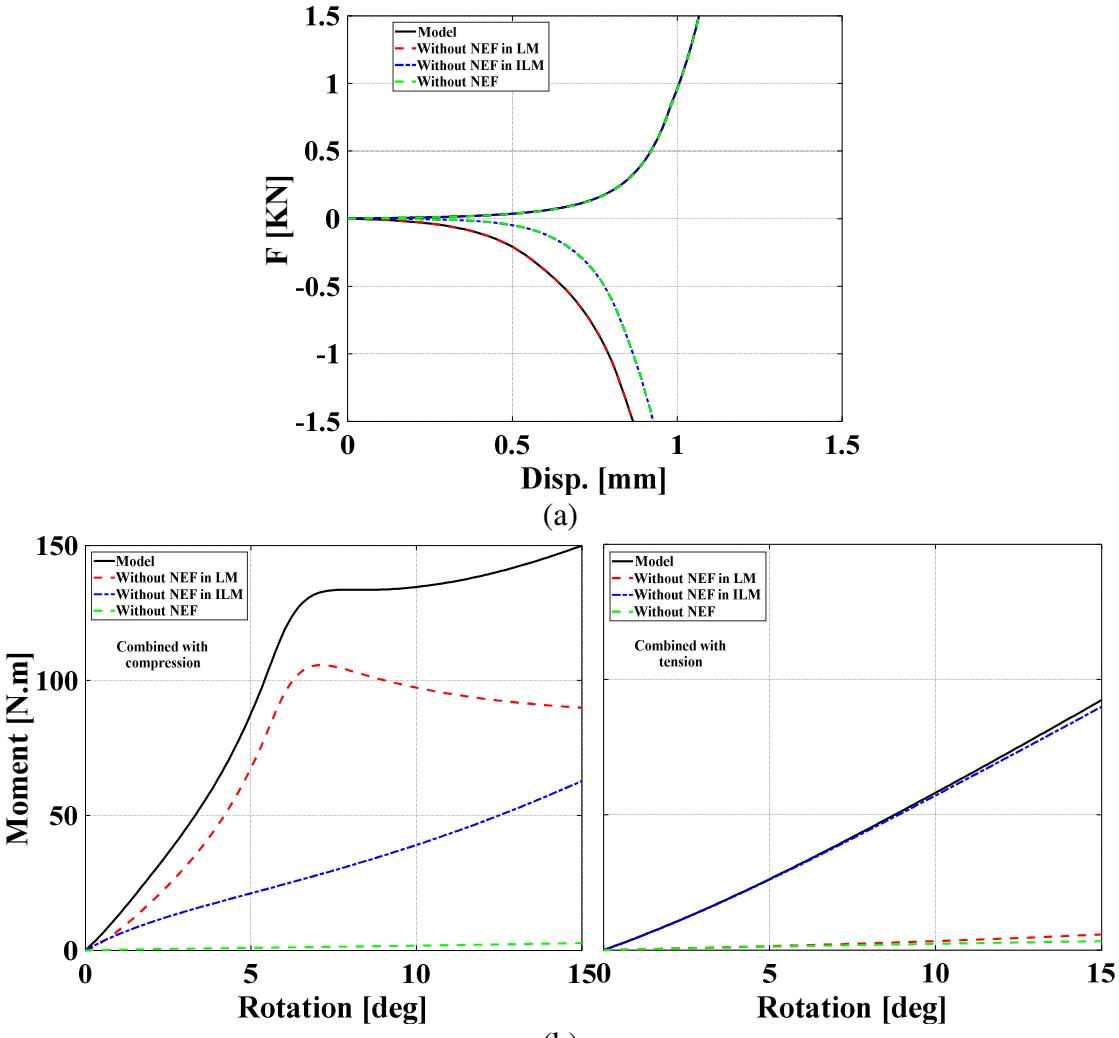

Figure 6. Influence of the LM/ILM collagen networks on the axially/torsionally disc response: (a) load curves and (b) moment curves.

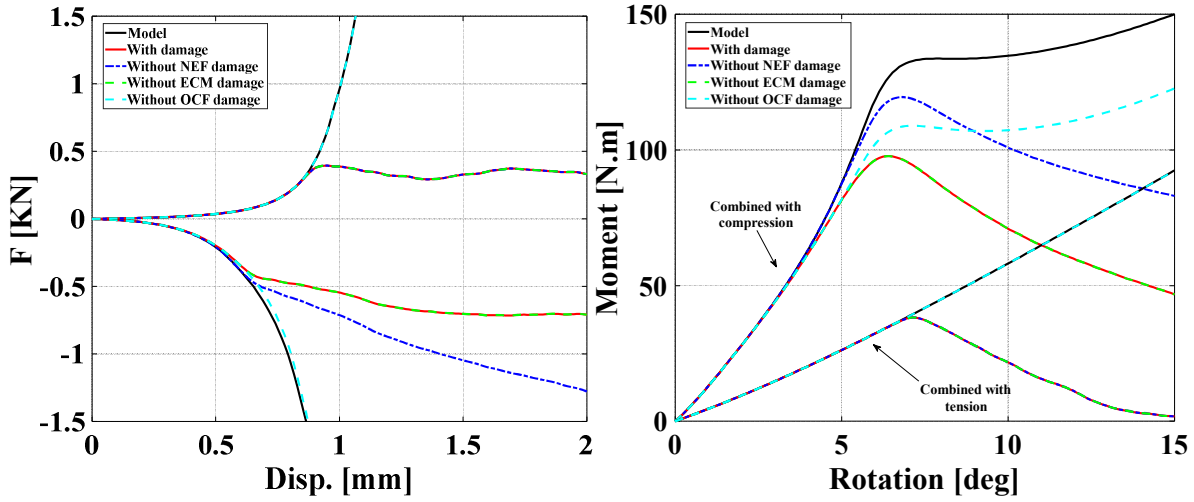

(a) (b)

Figure 7. Influence of the damage events on the axially/torsionally disc response: (a) load curves and (b) moment curves.

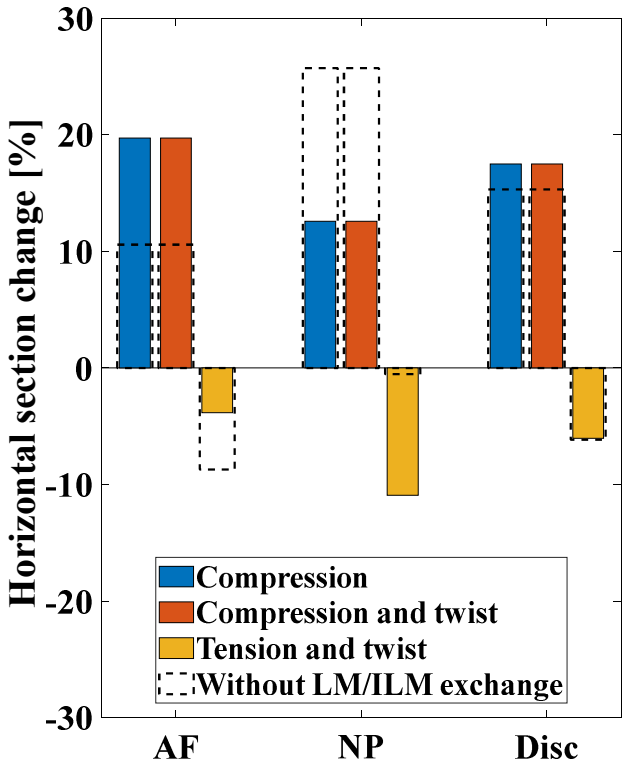

Figure 8. Influence of the LM/ILM fluid exchange on the horizontal section change under different loading conditions (AF: Annulus fibrosus, NP: nucleus pulposus). The disc is axially loaded at 1.1 mm and twisted at 7°.

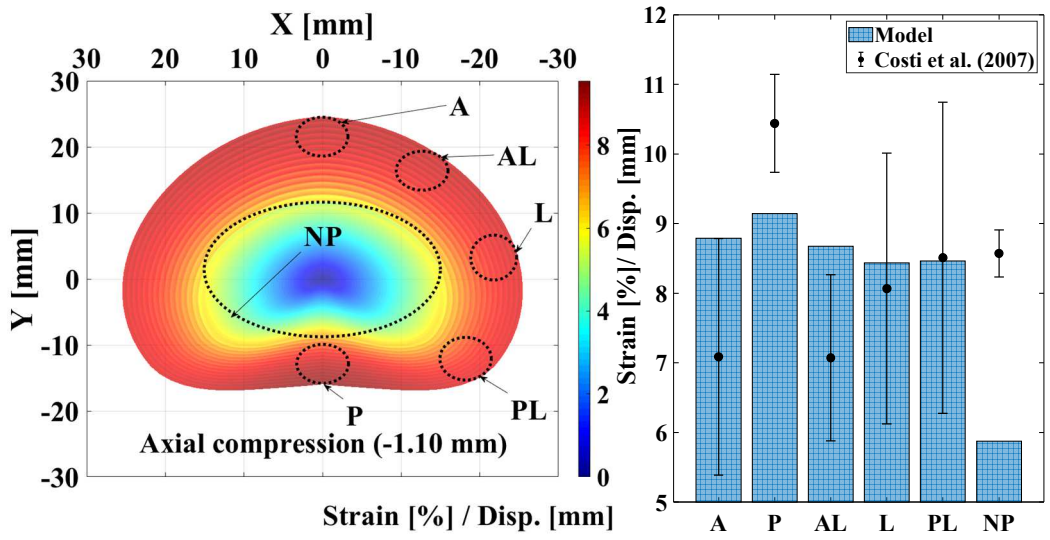

(a)

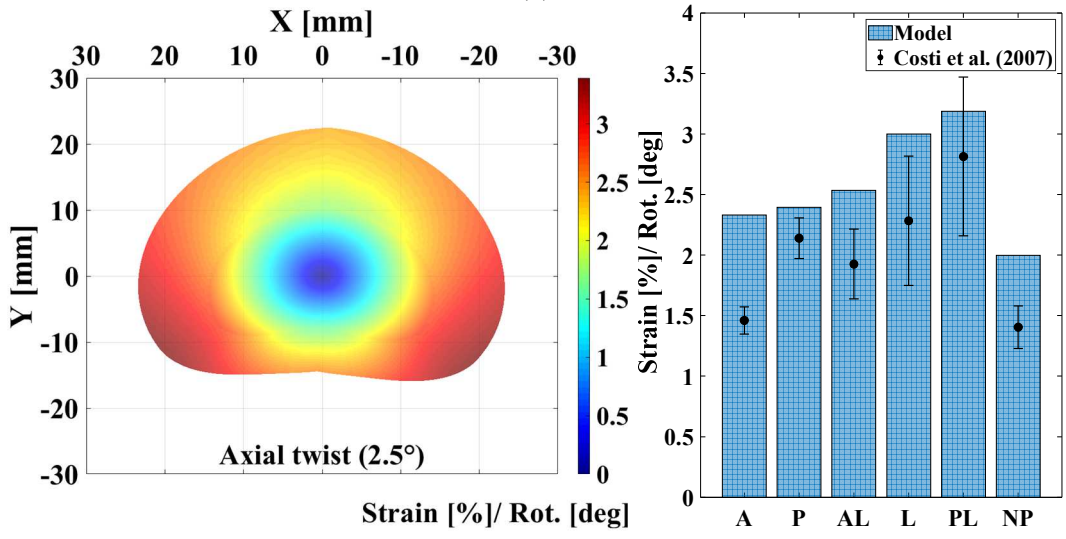

(b)

Figure 9. Predicted normalized radial strains (%/mm) in a disc (a) compressed at 1.1 mm and (b) twisted at 2.5°. The comparison to Costi et al. [52] data is performed for different regions in which the local strains are averaged (A: Anterior, P: Posterior, AL: Anterior-Lateral, L: Lateral, PL: Posterior-Lateral, NP: nucleus pulposus).

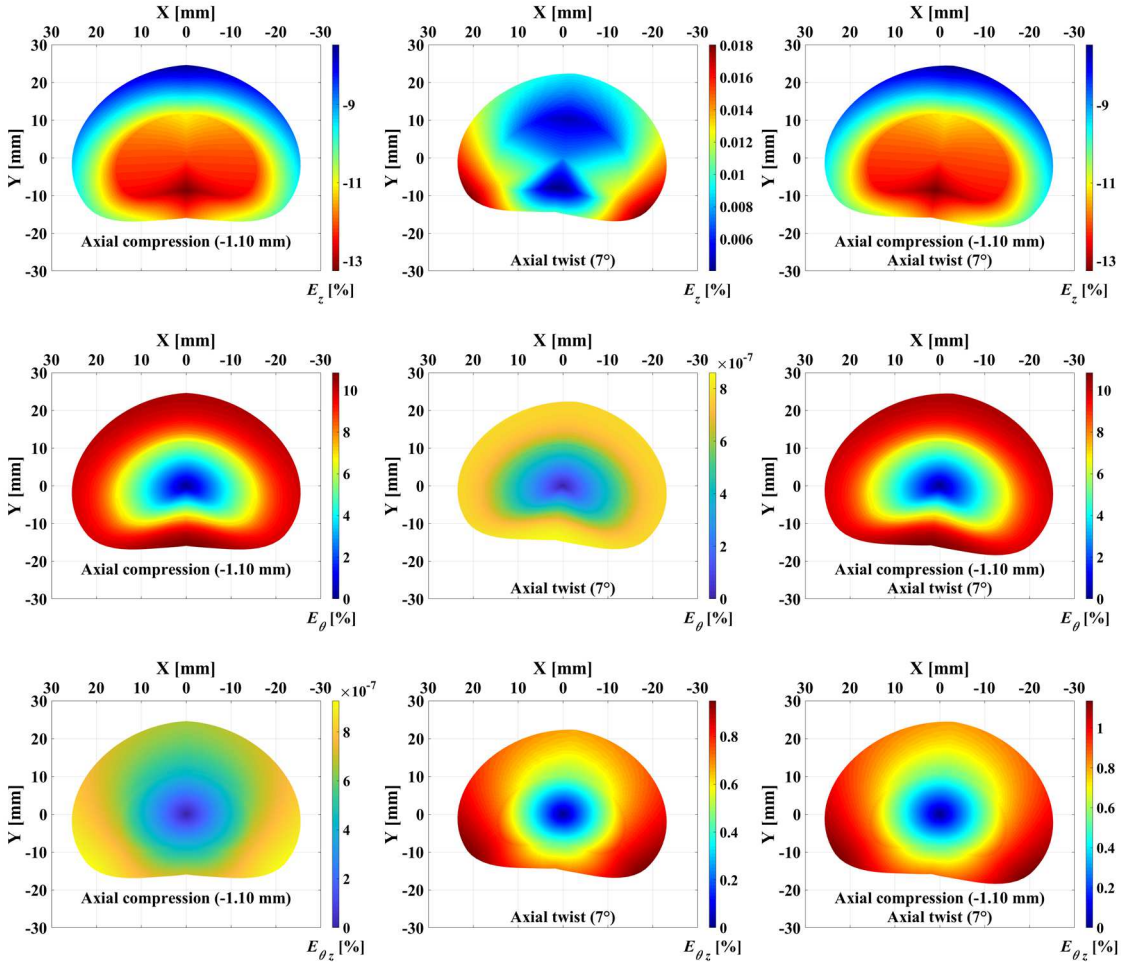

Figure 10. Contour plots of the local axial, circumferential and shear strains E_z, E_θ and $E_{\theta z}$ in axially/torsionally loaded discs.

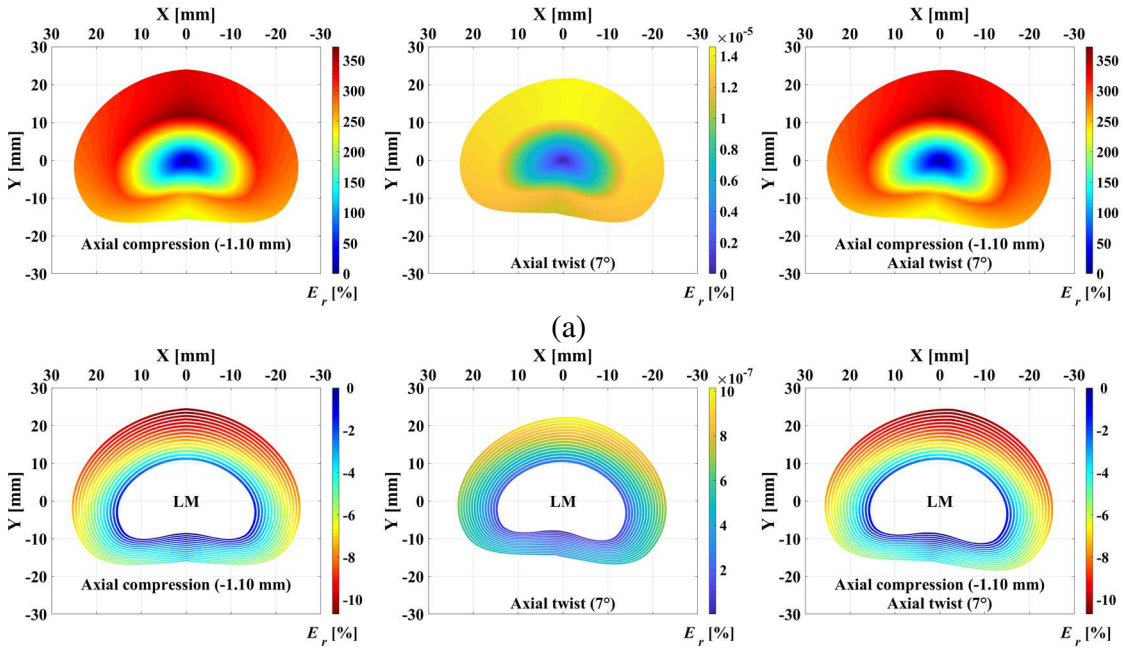

Figure 11. Contour plots of the local radial strain E_r in axially/torsionally loaded discs: (a) in ILM, (b) in LM.

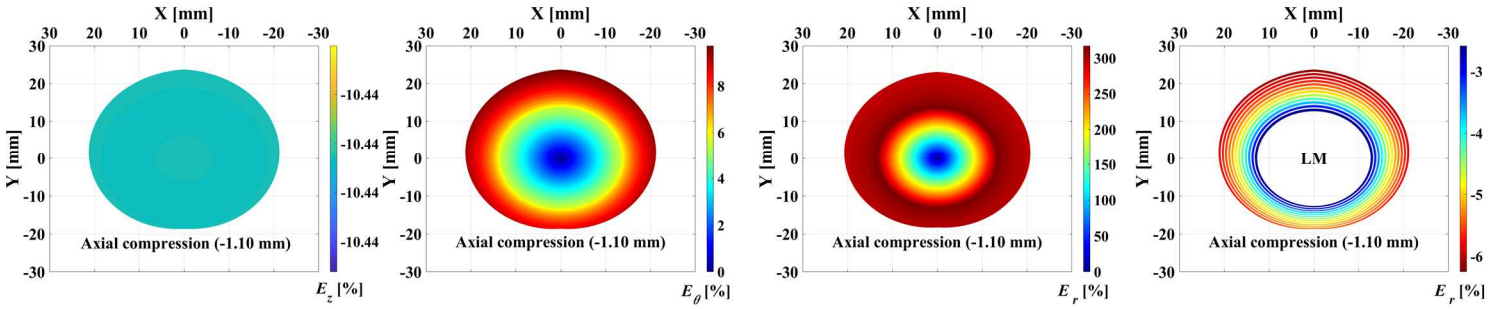

(a)

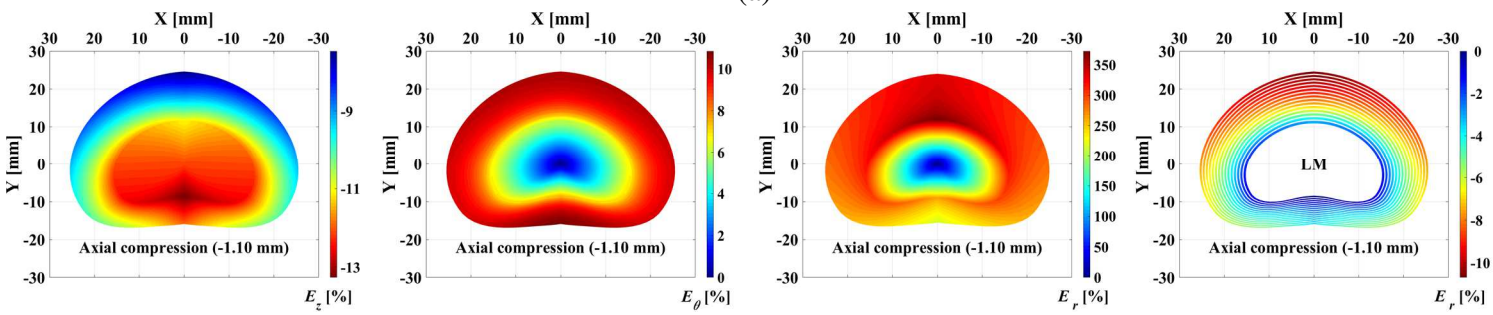

(b)

Figure 12. Morphology influence on the local strains local axial, circumferential and radial strains E_z, E_θ and E_r (in ILM and in LM) in compressed discs: (a) simplified disc morphology in circular basis with $R^0_{sagittal} = R^0_{frontal}$ (all initial heights and OCF orientations in Table 1 are averaged), (b) actual disc morphology.

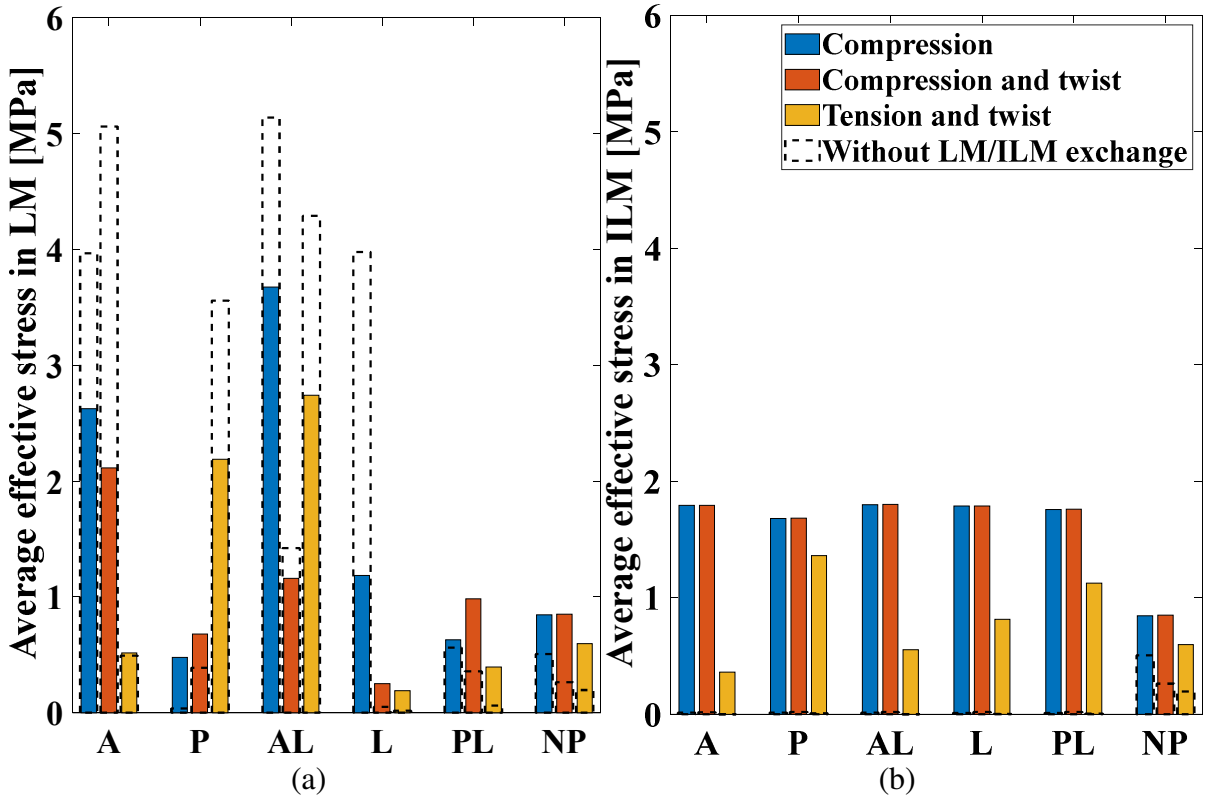

Figure 13. Influence of the LM/ILM fluid exchange on the local effective stress averaged in the different disc regions under different loading conditions (A: Anterior, P: Posterior, AL: Anterior-Lateral, L: Lateral, PL: Posterior-Lateral, NP: nucleus pulposus). The disc is axially loaded at 1.1 mm and twisted at 7°.

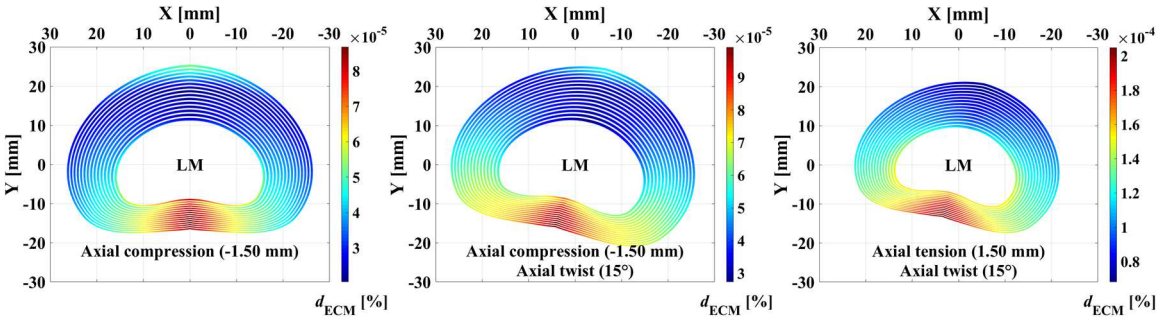

(a)

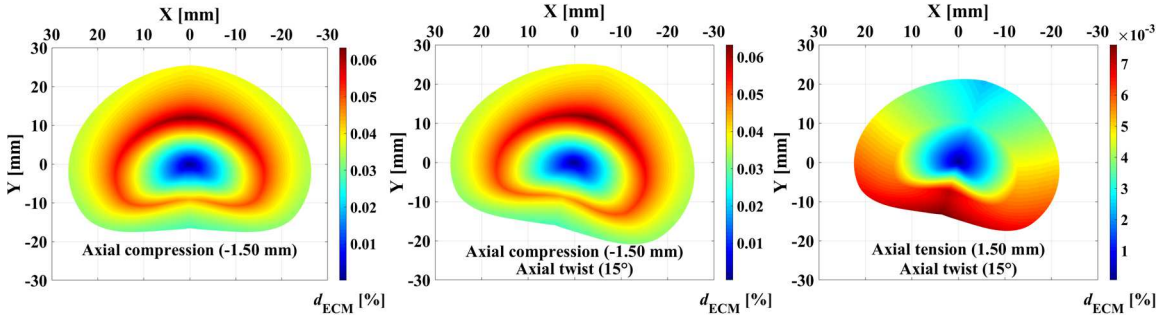

(b)

Figure 14. Contour plots of the ECM damage d_{ECM} in axially/torsionally loaded discs: (a) in LM, (b) in ILM.

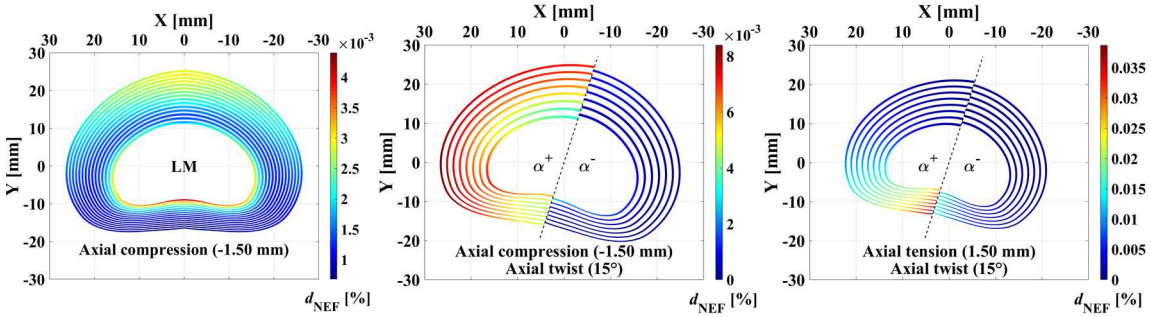

(a)

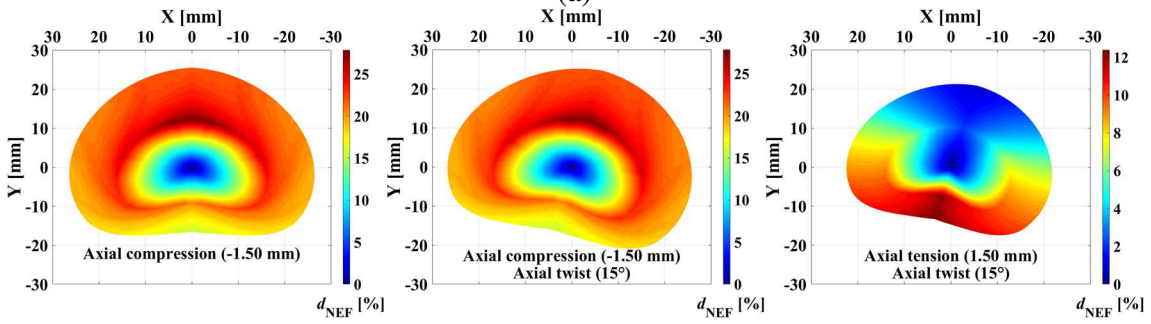

(b)

Figure 15. Contour plots of the NEF damage d_{NEF} in axially/torsionally loaded discs: (a) in LM, (b) in ILM.

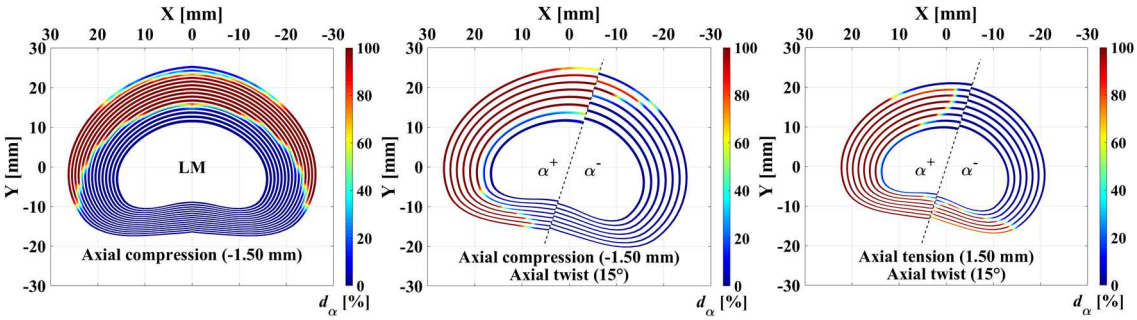

Figure 16. Contour plots of the OCF damage d_α (in LM) in axially/torsionally loaded discs.

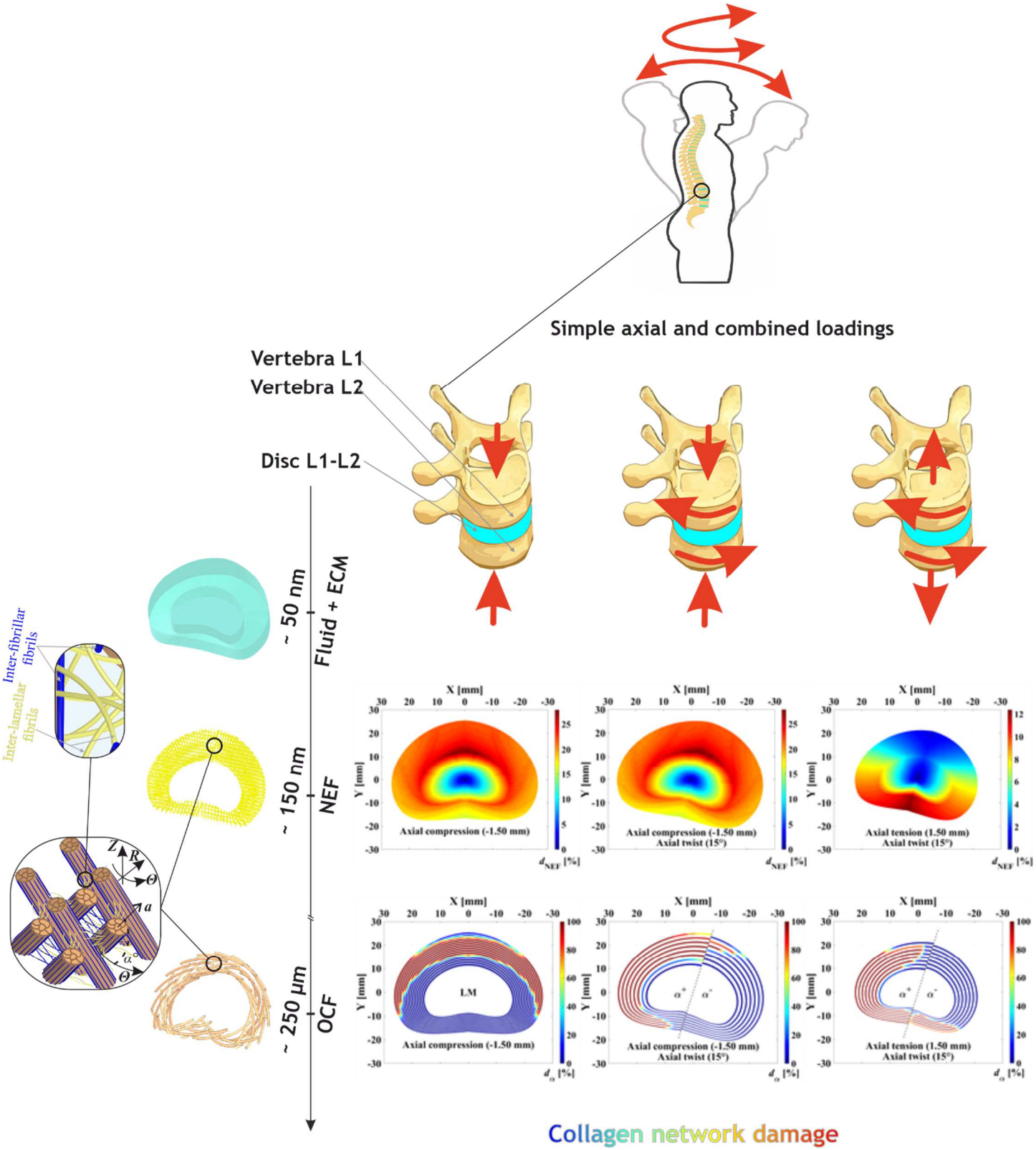
Simple axial and combined loadings
Vertebra L1
Vertebra L2
Disc L1-L2
~ 50 nm
Fluid + ECM
~ 150 nm
NEF
~ 250 µm
OCF
Inter-fibrillar fibrils
Inter-lamellar fibrils
Axial compression (-1.50 mm)
Axial compression (-1.50 mm) Axial twist (15°)
Axial tension (1.50 mm) Axial twist (15°)
LM
Collagen network damage